Determining the refractive index of highly scattering media by means of imaging with an ellipsometric setup

Masterarbeit der Philosophisch-naturwissenschaftlichen Fakultät
der Universität Bern

vorgelegt von
Patrick Stähli

2017

Leiter der Arbeit
Prof. Dr. M. Frenz

Abstract

Determining the complex refractive index of highly scattering media by means of applying Fresnel's equations can be challenging. This is attributable to three main difficulties: First, the directly specularly reflected beam needs to be distinguished from the backscattered light. Secondly, the angle between the media's surface normal and the illumination beam's propagation direction has to be measured in a precise manner in order to achieve reasonable results. Finally, the media's surface roughness has a big impact on the kind of reflection and therefore, in order to apply Fresnel's equations, this issue needs to be taken into account.

In this Master thesis, a compact and inexpensive imaging system was developed to circumvent this issues. An ellipsometry based setup was built and optimized in order to be able to measure the refractive index of highly scattering media independent of the illumination beam's intensity and angle of incidence. The applicability thereof has been ascertained with experiments on highly concentrated colloidal latex suspensions. The real part of the refractive index was measured with a deviation from literature of only a few tenth of a percent over a wide range of particle concentrations.

In a second step, the effect of surface roughness was investigated by performing Monte Carlo simulations. These simulations revealed that the developed data analysis is promising to give reliable results in real measurements.

Contents

Chapter 1

Introduction

The interaction of light with matter is described by optical parameters, *i.e.*, the refractive index n, the transport mean free path $l^\star$, the absorption coefficient μ_a, the scattering coefficient μ_s and scattering laws. In light propagation studies, accurate assessment of a samples optical properties is essential in order to conduct light propagation experiments in a relevant manner.

Further, studying the interaction of light with tissues is relevant in many fields, among which the development of diagnostic tools based on refractive index measurements is promising. This can be attributed to the fact that the refractive index differs for different tissue types [1].

As described later on in this thesis, a sample's refractive index can be determined by analysing its reflectivity. However, direct reflectivity measurements for highly scattering media, *e.g.* tissues, turned out to be challenging for two main reasons:

- When illuminating a highly scattering sample, only a minor part of illumination beam is reflected directly, whereas a major part enters into the sample. This part is then, due to dominating multiple scattering, backscattered from the sample diffusely and overlaid on the directly reflected part. When measuring a sample's refractive index by analysing its directly reflected light, the latter needs to be filtered out from the sample's backscattered light.

- Many samples, especially tissue samples, have a rough surface. As a consequence, the reflection turns out to be diffuse. In order to determine a sample's refractive index from this diffuse reflection, the sample's surface roughness needs to be taken into account.

Several groups circumvent these issues by either preparing the sample in a way that the backscattering effects and surface roughness are negligible [2, 3] or by developing theoretical models to correct *ex post* for the backscattering effects [4]. However, during a sample preparation process, the sample's optical properties might change. Further, a sample preparation to the desired extent can not always be achieved,

i.e. in-vivo measurements. In contrast, accounting for the backscattering effects by developing theoretical models, several approximations about the sample need to be made.

In this Master's thesis, a compact setup in order to perform expeditious refractive index measurements for highly scattering samples without any sample preparation is presented. Further, in a preliminary study, the effect of surface roughness to the refractive index measurements was investigated.

Chapter 2 gives a short overview on how the light is modelled by electromagnetic waves, a mathematical formalisation of light polarisation and a derivation of the complex refractive index $\mathcal{N}$ starting from Maxwell's equations. Further, Snell's law and the Fresnel equations are discussed.

Chapter 3 describes the measurement setup that I have developed and which works in reflection mode. Further, an error estimation study reveals the expected accuracy limits using such a setup.

Chapter 4 details the optimisation process carried out during this Master's project: three different variations of the setup and data-analysis are shown. The samples under investigation were either fluids or prepared in a way that the surface roughness was negligible and therefore, specular reflection achieved.

Chapter 5 investigates the effect of surface roughness in reflectivity measurements and a data-analysis in order to circumvent this issue is introduced. In order of assess the feasibility of this approach, a Monte Carlo simulation study was performed.

Chapter 2

Theoretical background

2.1 Light Modelled by Electromagnetic Waves

In 1865, James Clerk Maxwell published his paper *A Dynamical Theory of the Electromagnetic Field*, where he derives the electromagnetic wave equation propagating with a velocity in close agreement to the speed of light measured by experiment. As a consequence, he deduced that light must be an electromagnetic wave. He assembled relationships between the electric and magnetic fields into a set of equations, today known as Maxwell's equations[1]: [5]

$$\nabla \cdot \vec{E} = \frac{\rho}{\epsilon_0} \qquad \qquad \text{Gauss' law} \qquad (2.1)$$

$$\nabla \cdot \vec{B} = 0 \qquad \qquad \text{Gauss' law for magnetism} \qquad (2.2)$$

$$\nabla \times \vec{E} = -\frac{\partial \vec{B}}{\partial t} \qquad \qquad \text{Faraday's law} \qquad (2.3)$$

$$\nabla \times \frac{\vec{B}}{\mu_0} = \epsilon_0 \frac{\partial \vec{E}}{\partial t} + \vec{J}. \qquad \qquad \text{Ampère's law} \qquad (2.4)$$

The electric and magnetic fields are represented by $\vec{E}$ and $\vec{B}$, respectively. ρ denotes the total charge density, which describes the charge per unit volume. The motion of charge density, namely the current density, is identified by $\vec{J}$. The constants ϵ_0 and μ_0 are the permittivity and permeability, respectively.

A general solution to the Maxwell's equations is the plane-wave approximation [5, 6]

$$\vec{E}(\vec{r}, t) = \vec{E}_0 \cdot e^{i(\vec{k} \cdot \vec{r} - \omega t)} \qquad (2.5)$$

where ω is the angular frequency and $\vec{k}$ wave number. The plane-wave describes the propagation of an electric field $\vec{E}$ in the direction of $\vec{k}$. At any arbitrary position in propagation direction, the amplitude of the electric wave is equal everywhere

---

[1]In Maxwell's paper, the equations were written without the modern vector notation, what makes them hardly understandable.

in the plane normal to the propagation direction (see Figure 2.1). Since in the plane-wave approximation, $\vec{k}$ and $\vec{E_0}$ are perpendicular and $\vec{k}$ specifies the wave's propagation direction, only two dimensions remain where the vector $\vec{E_0}$ is confined. For simplicity, the coordinate system is oriented with the Z-axis in $\vec{k}$-direction. As a consequence, the wave vector becomes $\vec{k} = k \cdot z$ and the plane-wave reduces to [7]

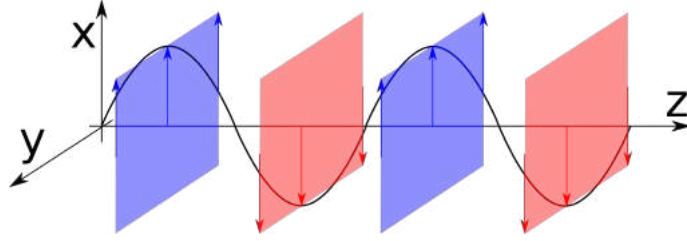$$\vec{E}(z,t) = \vec{E_0} \cdot e^{i(k \cdot z - \omega t)} \tag{2.6}$$

Figure 2.1: Sketch of the plane wave approximation. The electromagnetic wave propagates in Z-direction and is linearly polarized in x-direction. The amplitude of the electric wave at any arbitrary position in propagation direction is equal everywhere in the plane normal to the propagation direction.

2.2 Light Polarisation

In equation 2.6, the amplitude vector $\vec{E_0}$ is composed of the two components, E_{0x} and E_{0y}:

$$\vec{E_0} = E_{0x}\hat{x} + E_{0y}\hat{y} \tag{2.7}$$

where $\hat{x}$ and $\hat{y}$ are the unit vectors in x- and y-direction, respectively. The polarisation of light is described by the relationship of E_{0x} and E_{0y} [5, 6, 7]. It is important to recognize that the description above is located in a local coordinate system whose Z-axis coincide with the waves propagation direction $\vec{k}$. Thus, the polarisation of a plane-wave is completely specified by two complex numbers arranged into a vector, called Jones vector [8, 9]:
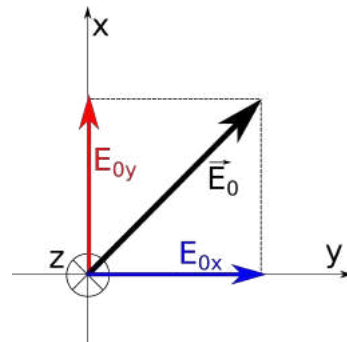

Figure 2.2: Sketch of the relationship between the two components E_{0x} and E_{0y} and the resulting amplitude vector $\vec{E_0}$.

$$|E_0\rangle = \begin{pmatrix} E_{x0} \\ E_{y0} \end{pmatrix} = e^{i\phi} \begin{pmatrix} e_x(t) \\ e_y(t) \end{pmatrix} \tag{2.8}$$

where $e_x(t)$ and $e_y(t)$ are the components of the Jones vector and the phase information is described by ϕ.

Every polarisation state can be described by the fundamental pairs of polarisation.

$$\begin{pmatrix} 1 \\ 0 \end{pmatrix} \quad \text{linearly polarised along x-axis} \tag{2.9}$$

$$\begin{pmatrix} 0 \\ 1 \end{pmatrix} \quad \text{linearly polarised along y-axis} \tag{2.10}$$

$$\begin{pmatrix} \cos(\alpha) \\ \sin(\alpha) \end{pmatrix} \quad \text{linearly polarised rotated through } \alpha \text{ from the x-axis} \tag{2.11}$$

$$\frac{1}{\sqrt{2}} \begin{pmatrix} 1 \\ -i \end{pmatrix} \quad \text{right circularly polarised} \tag{2.12}$$

$$\frac{1}{\sqrt{2}} \begin{pmatrix} 1 \\ i \end{pmatrix} \quad \text{left circularly polarised} \tag{2.13}$$

Clark Jones introduced a efficient formalism for the analysis of light propagation through optical elements, which are represented by 2×2 complex matrix operators $\mathcal{O}$ [8, 9]. These operators are called Jones matrices which act on the input polarisation state $|E_{in}\rangle$ and produce an output state $|E_{out}\rangle$:

$$|E_{out}\rangle = \mathcal{O}\,|E_{in}\rangle \tag{2.14}$$

The output state $|E_{out}\rangle$ of a state propagating through an array of multiple elements is given by matrix multiplication:

$$|E_{out}\rangle = \mathcal{O}\,|E_{in}\rangle = \mathcal{O}_n...\mathcal{O}_2\mathcal{O}_1\,|E_{in}\rangle \tag{2.15}$$

In the following list, the Jones matrix of commonly used optical elements are given [7]

Linear polariser

$$\begin{bmatrix} \cos^2(\theta) & \sin(\theta)\cos(\theta) \\ \sin(\theta)\cos(\theta) & \sin^2(\theta) \end{bmatrix} \tag{2.16}$$

Quarter-wave plate

$$\begin{bmatrix} \cos^2(\theta) + i\sin^2(\theta) & \sin(\theta)\cos(\theta) - i\sin(\theta)\cos(\theta) \\ \sin(\theta)\cos(\theta) - i\sin(\theta)\cos(\theta)) & \sin^2(\theta) + i\cos^2(\theta) \end{bmatrix} \tag{2.17}$$

Half-wave plate

$$\begin{bmatrix} \cos(2\theta) & \sin(2\theta) \\ \sin(2\theta) & -\cos(2\theta) \end{bmatrix} \tag{2.18}$$

θ represents the transmission axis with respect to the X-axis for polarisers and for the quarter- and half-plate, the angle θ refers to the angle of the fast axis with respect to the X-axis.

Reflection

$$\begin{bmatrix} -r_p & 0 \\ 0 & r_s \end{bmatrix} \tag{2.19}$$

Transmission

$$\begin{bmatrix} t_p & 0 \\ 0 & t_s \end{bmatrix} \tag{2.20}$$

Here, r_p, t_p , r_s t_s are the Fresnel coefficients for P- and S-Polarisation, which are derived in section 2.4. For any incident beam, the polarisation state parallel to the plane of incidence is called P-Polarisatin. Likewise, S-Polarisation is the polarisation state perpendicular to the plane of incidence.
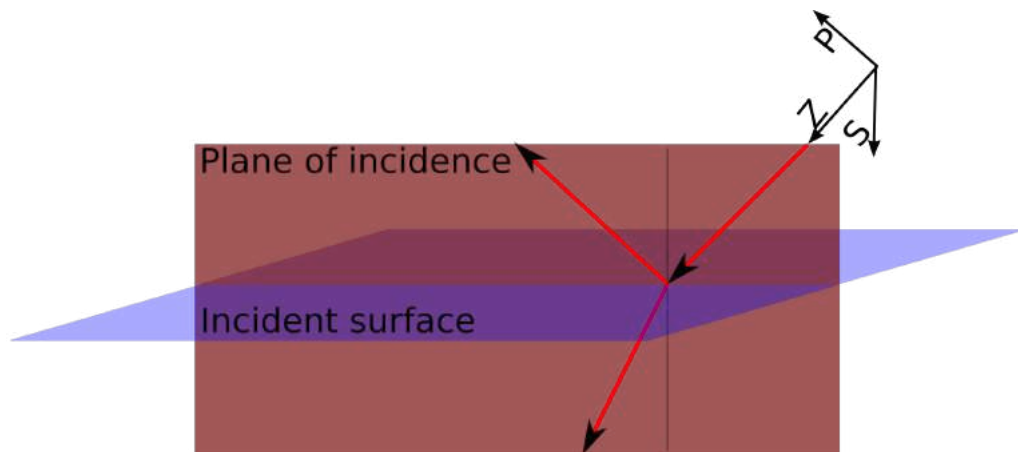

Figure 2.3: The polarisation states P and S are defined by their relative orientation to the plane of incidence.

2.3   Index of Refraction of an effective medium

The refractive index is an important optical property which describes, among others, the interaction of light with matter. It is composed of a real part n_r, which attributes the ratio of the speed of light in vacuum and matter, and an imaginary part n_i, which defines the absorption coefficient $\mu_a = 2\omega n_i/c$. However, for many materials, quantities such as the electric conductivity, the susceptibility or elastic modulus vary in space. One category which fall into that category are tissues, which consists blood vessels, skin cells, fat enclosures etc. Such a macroscopically inhomogeneous medium is usually treated as an effective medium which approximates the overall optical constances as the mean of the whole inhomogeneous media [11]. In this thesis, all the samples are treated as effective-media. Further, in a first approximation, tissues are predominately made of water. Thence, tissues can be treated as dielectrics where the containing charge carriers are bound. As a consequence, dielectrics are weak electric conductors and the effect of a magnetic field is negligible.

However, a very straight forward approach to derive the refractive index of dielectrics is based on the electric polarisation.

2.3.1   Electric Polarisation

An idealized model of a dielectric is assumed, where small conducting spheres are symmetrically surrounded by an opposite charge *e.g.* atoms, which are built of a positive charged core surrounded by negative charged bound electrons. As long as no external electric file is applied to the dielectric, the positive and negative point charge coincide and the net charge is zero. Once an electric field is applied to the dielectric, the atoms gain electric dipole moment by displacing the positive and negative charges and the dielectric is said to be electrically polarised. The dipole moment $\vec{p}$, as a measure of the charge separation, is described as follows [5]:

$$\vec{p} = q \cdot \vec{d} \tag{2.21}$$

where $\vec{d}$ is the displacement vector pointing from the negative to the positive charge q. However, by definition, the electric polarisation of a dielectric is the electric dipole moment induced per unit volume [6].

$$\vec{P} = N \cdot q \cdot \vec{d} = N \cdot \vec{p} \tag{2.22}$$

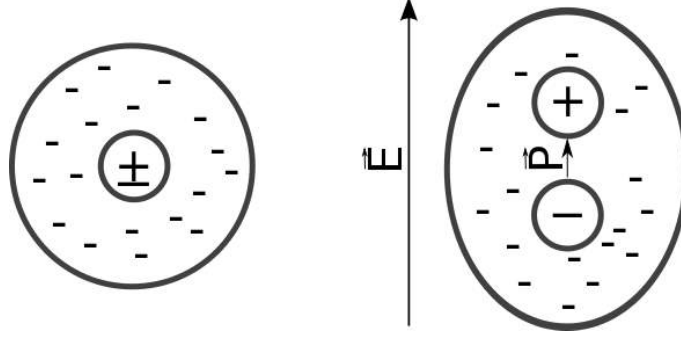Here, N denotes the number of atoms in the unit volume.

Figure 2.4: Left: The positive charged core and the negative charged bound electrons coincide. Right: In the presence of an electric field, the charge distributions are separated by a distance $\vec{d}$.

However, in a linear, homogeneous and isotropic medium, the intensity of the $\vec{P}$ field is linearly proportional to the intensity of the $\vec{E}$ field [10]:

$$|P|^2 = \epsilon_0 \cdot \chi(\omega) \cdot |E|^2 \tag{2.23}$$

As for ϵ_0, it designates the electric field constant and $\chi(\omega)$ is called the electric susceptibility, which depends on the frequency ω of the E-Field. This dimensionless complex constant indicates the degree of electric polarization of a dielectric in response to an applied E-Field.

As a consequence, the resulting P-Field in the dielectric is uniformly distributed when a constant, uniformly distributed E-Fields is applied (See fig. 2.5).
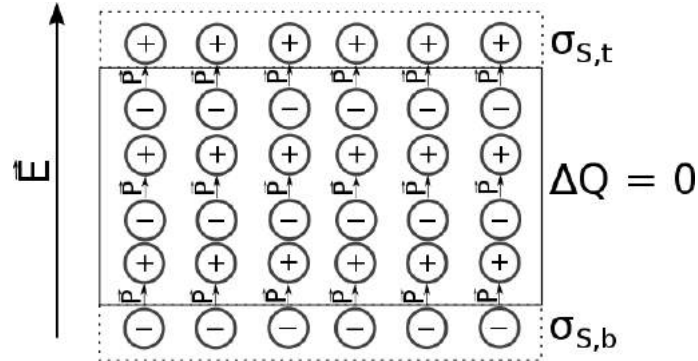
Figure 2.5: Uniformity of the P-Field by applying a constant E-Field on dielectrics.

The amount of charges appearing at the surface of an arbitrary volume within the dielectric is then the product of the number density of charges N, the area's surface A and the displacement vector $\vec{d}$. Therefore, the resulting surface charge density $d\sigma_s = dq/dA$ is described by the following equation:

$$\sigma_s = \frac{A \cdot \vec{d} \cdot N \cdot q}{A} = \vec{P} \tag{2.24}$$

Plugging these equation into the definition of the polarisation vector (Eq. 2.22), the surface charge density σ_s turns out to be proportional to the magnitude of the

polarisation. As shown in figure 2.6, only the part of the displacement vector normal to the surface has an impact on σ_s:

$$\sigma_s = \vec{P} \cdot \vec{n} \tag{2.25}$$

Since the surface charge has the same magnitude but different signs at opposite sites of a volume, the resulting charge caused by polarization ΔQ within any volume is zero (see Figure 2.5). However, in a more general case, the electric field $\vec{E}$ is not uniformly distributed and consequently, according to equation 2.23, the resulting polarisation field $\vec{P}$ is not uniformly distributed either. This leads to a non-zero charge

Figure 2.6: Sketch of the polarisation effect by an E-Field applied not normal to the dielectrics surface.

ΔQ within the volume. To remember the fact, that this charge is caused by polarisation, it is called polarisation charge Q_{Pol} (see Figure 2.7).
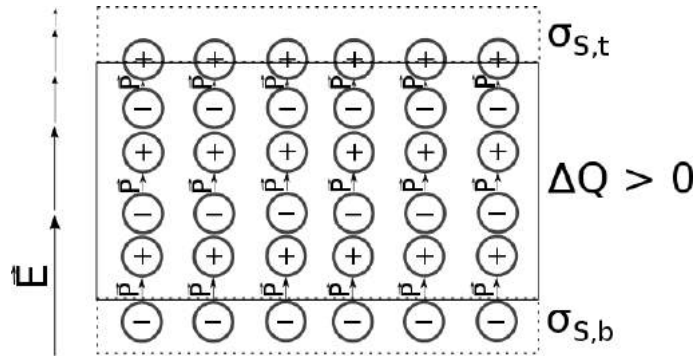
Figure 2.7: Sketch of the P-Field in a dielectric on which a non uniformly E-Field is applied.

In the most general case, treating an arbitrary shape of the volume, it's polarisation charge Q_{Pol} is equal the negative sum of all surface charges. Therefore, the polarisation charge Q_{Pol} is negative the surface integral of the surface charge densities σ_s:

$$Q_{pol} = - \int_S \sigma_s \, ds \overset{2.25}{=} - \int_S \vec{P} \cdot \vec{n} \, ds \tag{2.26}$$

On the other hand, the total charge inside this volume is composed of every single charge within these volume:

$$Q_{Pol} = \int_V \rho_{pol} \, dV \tag{2.27}$$

where ρ_{pol} describes the polarisation charge density. Combining these two equations and applying Gauss's divergence theorem, a relation between the charge density and

the divergence of the P-Field is found:

$$\int_V \rho_{pol} \, dV = -\int_S \vec{P} \cdot \vec{n} \, ds \overset{\text{Gauss}}{=} -\int_V \nabla \cdot \vec{P} \, dV \tag{2.28}$$

$$\Rightarrow \rho_{pol} = -\nabla \cdot \vec{P} \tag{2.29}$$

Meaning, in a non uniformly distributed P-Field within an arbitrary volume, the polarisation charge within this volume is found to be equal to the divergence of the P-Field.

However, a moving charge density induces always a current density [5, 6]. The current density J is defined as the current's intensity I per area A, where I is the time derivative of the total electric charge:

$$J = \frac{I}{A} = \frac{1}{A}\frac{dQ}{dt} = \frac{1}{A}\frac{dQ}{dV}\frac{dV}{dt} = \frac{1}{A} \cdot N \cdot q \cdot \frac{A \cdot dx}{dt} = N \cdot q \cdot \frac{dx}{dt} \tag{2.30}$$

In combination with equation 2.22, the polarization current density J_{pol} is found to be:

$$J_{pol} = \frac{d\vec{P}}{dt} \tag{2.31}$$

2.3.2 From Maxwell's Equations to the Complex Index of Refraction

Having an appropriate description of the polarisation charge and current density, ρ_{pol} and J_{pol}, respectively, the refractive index is derived form Maxwell's equation for isotropic materials:

$$\nabla \cdot \vec{E} = \frac{\rho}{\epsilon_0} \qquad\qquad \text{Gauss' law} \tag{2.32}$$

$$\nabla \cdot \vec{B} = 0 \qquad\qquad \text{Gauss' law for magnetism} \tag{2.33}$$

$$\nabla \times \vec{E} = -\frac{\partial \vec{B}}{\partial t} \qquad\qquad \text{Faraday's law} \tag{2.34}$$

$$\nabla \times \frac{\vec{B}}{\mu_0} = \epsilon_0 \frac{\partial \vec{E}}{\partial t} + \vec{J} \qquad\qquad \text{Ampère's law} \tag{2.35}$$

Here, ρ and $\vec{J}$ are the total charge and current densities, respectively. These quantities are composed of different terms:

- $\left.\begin{matrix} J_{free} \\ \\ \rho_{free} \end{matrix}\right\}$ Arises from free charges in motion such as e$^-$ in metal

- $\begin{rcases} J_{pol} \\ \rho_{pol} \end{rcases}$ Arises from the polarization of the medium

- $\begin{rcases} J_{other} \\ \rho_{other} \end{rcases}$ All other effects $e.g$ interal currents exhibited by atoms.

For the sake of convenience and since biological tissues can be approximated as dielectrics, only dielectric materials are considered. Therefore, the charge and current density, ρ_{free} and J_{free} respectively, are assumed to be zero. Further, all other effects, as for example the internal currents of the atoms, are assumed to be small compared to the polarisation charge and current density and are therefore neglected too [7]. Thence, considering only the charge and current density which arises from polarisation, the Maxwell's equation are written as follows:

$$\nabla \cdot \vec{E} = \frac{\rho}{\epsilon_0} \overset{2.29}{=} -\frac{\nabla \cdot \vec{P}}{\epsilon_0} \qquad\qquad \text{Gauss' law} \qquad (2.36)$$

$$\nabla \cdot \vec{B} = 0 \qquad\qquad \text{Gauss' law for magnetism} \qquad (2.37)$$

$$\nabla \times \vec{E} = -\frac{\partial \vec{B}}{\partial t} \qquad\qquad \text{Faraday's law} \qquad (2.38)$$

$$\nabla \times \frac{\vec{B}}{\mu_0} = \epsilon_0 \frac{\partial \vec{E}}{\partial t} + \vec{J} \overset{2.31}{=} \epsilon_0 \frac{\partial \vec{E}}{\partial t} + \frac{\partial \vec{P}}{\partial t} \qquad\qquad \text{Ampère's law} \qquad (2.39)$$

To obtain the wave-equation of the electric field from Maxwell's equation, a few mathematical steps have to be done starting by taking the curl of Faraday's law:

$$\nabla \times (\nabla \times \vec{E}) = \nabla \times (-\frac{\partial \vec{B}}{\partial t}) \qquad (2.40)$$

$$\overset{2.45}{=} -\nabla^2 \vec{E} + \nabla(\nabla \cdot \vec{E}) = \nabla \times (-\frac{\partial \vec{B}}{\partial t}) \qquad (2.41)$$

$$\overset{2.39}{=} -\nabla^2 \vec{E} + \nabla(\nabla \cdot \vec{E}) = -\frac{\partial}{\partial t} \left(\epsilon_0 \mu_0 \frac{\partial \vec{E}}{\partial t} + \mu_0 \cdot \frac{\partial \vec{P}}{dt} \right) \qquad (2.42)$$

$$\overset{2.36}{=} -\nabla^2 \vec{E} - \frac{1}{\epsilon_0}\nabla(\nabla \cdot \vec{P}) = -\epsilon_0 \mu_0 \frac{\partial^2 \vec{E}}{\partial t^2} - \mu_0 \frac{\partial^2 \vec{P}}{\partial t^2} \qquad (2.43)$$

$$= \nabla^2 \vec{E} - \epsilon_0 \mu_0 \frac{\partial^2 \vec{E}}{\partial t^2} = \mu_0 \frac{\partial^2 \vec{P}}{\partial t^2} - \frac{1}{\epsilon_0}\nabla(\nabla \cdot \vec{P}) \qquad (2.44)$$

Where in the first step, the following identity was used [12]

$$\left(\nabla \times (\nabla \times \vec{A}) \right) = \nabla \cdot (\nabla \cdot \vec{A}) - \nabla^2 \cdot \vec{A} \qquad (2.45)$$

Equation 2.44 is an inhomogeneous wave-equation. The source term on the right hand site of the wave-equation arises from the medium's polarisation induced by

an external electric field. One solution to this wave equation is the plane-wave approximation (see Equ. 2.6). This approximation is appropriate, as long as the spatial extent of the observed dielectric is much smaller than the spatial extent of the electric field. Applying this plane-wave approximation to the dielectric described in section 2.3.1, the charge density $\sigma_{s,t}$ at the border of an arbitrary volume is equal to the negative charge density at the opposite side of the volume $\sigma_{s,b}$ (see Figure 2.8). Further, no sources or sinks occur. Consequently, the divergence of the polarization field $\vec{P}$, induced by the electric field $\vec{E}$ propagating in z-direction is zero:

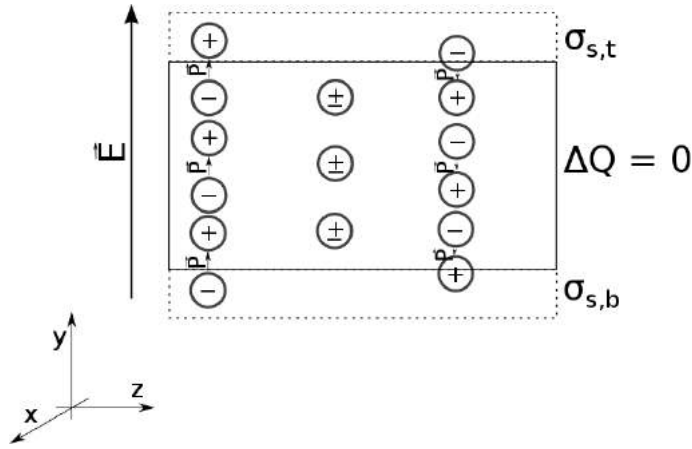$$\nabla \cdot \vec{P} = 0 \tag{2.46}$$

Figure 2.8: Sketch of the behaviour of a dielectric in the presence of an electromagnetic plane wave. According to the plane-wave approximation, the amplitude of the electromagnetic filed at every point in z-direction equal in y-direction. Therefore, the polarization $\vec{P}$ is independent of the y-direction.

Hence, thanks to the plane-wave approximation, the wave equation 2.44 reduces to:

$$\nabla^2 \vec{E} - \epsilon_0 \mu_0 \frac{\partial^2 \vec{E}}{\partial t^2} = \mu_0 \frac{\partial^2 \vec{P}}{\partial t^2} - \frac{1}{\epsilon_0} \nabla(\nabla \cdot \vec{P}) \tag{2.47}$$

$$\stackrel{2.46}{=} \nabla^2 \vec{E} - \epsilon_0 \mu_0 \frac{\partial^2 \vec{E}}{\partial t^2} = \mu_0 \frac{\partial^2 \vec{P}}{\partial t^2} \tag{2.48}$$

As described in section 2.3.1, the amplitude of the polarisation is assumed to be linearly proportional to the amplitude of the electric field with a complex proportionality factor $\chi(\omega)$, called susceptibility. However, equation 2.23 implies that the angular frequency of the plane-wave equation of the polarisation is equal to the angular frequency of the electric plane-wave:

$$P_y = P_0 \cdot e^{i(kz - \omega t)} \tag{2.49}$$

Putting the plane wave approximation of the electric field and the polarization field into equation 2.48, the dispersion relation is found:

$$\nabla^2 \vec{E} - \epsilon_0 \mu_0 \frac{\partial^2 \vec{E}}{\partial t^2} = \mu_0 \frac{\partial^2 \vec{P}}{\partial t^2} \tag{2.50}$$

$$\overset{2.44}{=}\overset{2.48}{} -E_0 k^2 \cdot e^{i(kz-\omega t)} + \epsilon_0 \mu_0 \omega^2 E_0 \cdot e^{i(kz-\omega t)} = -\mu_0 \omega^2 P_0 \cdot e^{i(kz-\omega t)} \tag{2.51}$$

$$= -E_0 k^2 + E_0 \epsilon_0 \mu_0 \omega^2 = -\mu_0 \omega^2 P_0 \tag{2.52}$$

$$\overset{2.23}{=} -k^2 + \epsilon_0 \mu_0 \omega^2 = -\mu_0 \omega^2 \epsilon_0 \chi \tag{2.53}$$

$$\Rightarrow k = \frac{\omega}{c}\sqrt{1+\chi} \tag{2.54}$$

The dispersion relation describes the relation between the wave number k and the angular frequency ω in a wave equation.

Since the susceptibility is a complex number, the term $\sqrt{1+\chi}$ is redefined as follows:

$$\sqrt{1+\chi(\omega)} = n(\omega) + i \cdot \kappa(\omega) = \mathcal{N}(\omega) \tag{2.55}$$

$\mathcal{N}(\omega)$ names the complex index of refraction. Thence, n is called the real part of the index of refraction and κ the complex part of the index of refraction. To visualize the meaning of the complex index of refraction $\mathcal{N}(\omega)$, the derived dispersion relation (Equ. 2.54 and Equ. 2.55) is put into the plane wave approximation of the electric field (Equ. 2.6):

$$E_y(z,t) = E_0 e^{i(k_z z - \omega t)} = E_0 e^{-\frac{\kappa \omega}{c}z} \cdot e^{i(\frac{n\omega}{c}z - \omega t)} \tag{2.56}$$

The complex part of the refractive index κ corresponds to a damping of the electric wave and is therefore related to the absorption coefficient of the considered medium. The absorption A of an electric wave is defined as the ratio of the intensity at point $z = z$ and the intensity at point $z = 0$ [13]:

$$A = \frac{E(z)^2}{E(0)^2} = e^{-(\mu_a \cdot z)} \tag{2.57}$$

where μ_a is called absorption coefficient of the medium. Using equation 2.56, the absorption coefficient is proportional to the complex part of the refractive index and the angular frequency of the electric wave:

$$\frac{E(z)^2}{E(0)^2} = e^{-(\mu_a \cdot z)}$$

$$\overset{2.56}{=} \frac{E_0 e^{-2\frac{\kappa\omega}{c}z} \cdot e^{2 \cdot i \frac{n\omega}{c}z} \cdot e^{-2 \cdot i\omega t}}{E_0 e^{-i\omega t}} = e^{-(\mu_a \cdot z)}$$

By comparison the coefficients, the following relation is found:

$$\mu_a = \frac{2\kappa\omega}{c} \tag{2.58}$$

However, the group velocity of a wave is given as the derivation of the angular frequency ω with respect to the wave number k [14]. Therefore, the real part of the complex refractive index n is the ratio of the wave velocity in vacuum and the wave velocity in the medium.

$$v = \frac{\partial \omega}{\partial k} = \frac{\partial \left(\frac{k \cdot c}{n} \right)}{\partial k} = \frac{c}{n} \tag{2.59}$$
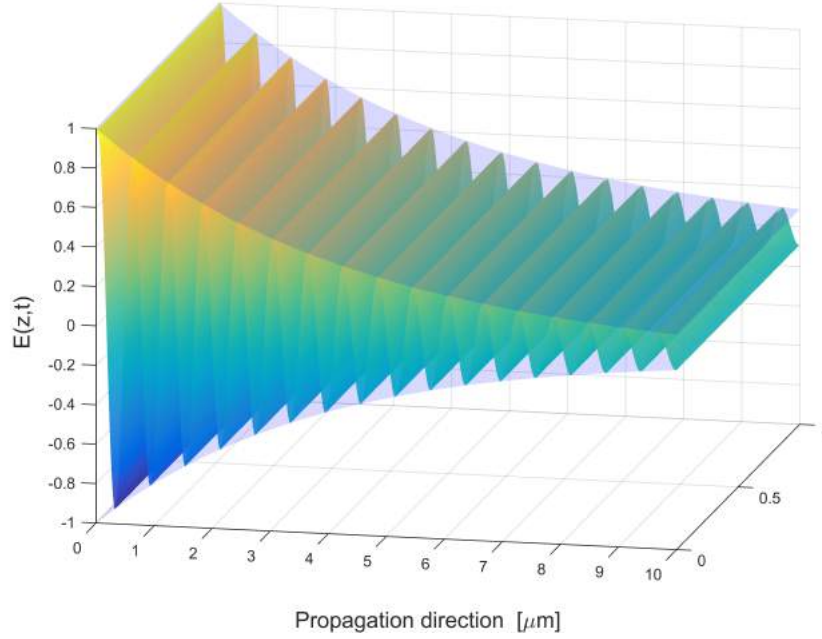
Figure 2.9: Visualization of a plane-wave propagating in Z-direction with a wavelength of $\lambda = 785$ nm and a complex refractive index $\mathcal{N} = 1.3 + i \cdot 0.03$.

Figure 2.9 represents a plane-wave with a wavelength of $\lambda = 785$ nm and a complex refractive index $\mathcal{N} = 1.3 + i \cdot 0.03$. It is clearly visible that the amplitude of the electric wave is reduced by $exp\left(-\kappa \omega z / c\right)$, as seen in figure 2.9 with the enclosure function.

2.4 Modelling the Refraction and Reflection of Light

Two different approaches are distinguished to model the refraction and reflection appearing at the boundary of two media with different refractive indices: (1) Snell's law, which describes the direction of the reflected and refracted beam and (2) the Fresnel's equations, modelling the intensities of these reflected and refracted beams in dependence of their polarisation direction.

2.4.1 Reflection/Refraction angles: Snell's Law

Starting from the plane-wave approximation for an depolarised electric wave, the incident wave E_1, the transmitted wave E_2 and the reflected wave E_3 are described as follows:

$$\vec{E}_1 = E_{0_1} \cdot e^{i(k_1 \cdot \vec{r}_1 - \omega_1 t)} \tag{2.60}$$

$$\vec{E}_2 = E_{0_2} \cdot e^{i(k_2 \cdot \vec{r}_2 - \omega_2 t)} \tag{2.61}$$

$$\vec{E}_3 = E_{0_3} \cdot e^{i(k_3 \cdot \vec{r}_3 - \omega_3 t)} \tag{2.62}$$

Since Maxwell's equations must hold also at the boundary between material 1 with a refractive index n_1 and material 2 with a refractive index n_2 [15, 16], the three equations 2.60, 2.61, 2.62 need to be equal.

$$\vec{E}_1 = \vec{E}_2 = \vec{E}_3 \tag{2.63}$$

By considering a reference frame, where x = 0 (see Figure 2.10) and splitting up the exponentials, this leads to two equations:

$$\vec{k}_1 \cdot \vec{r}\,|_{x=0} = \vec{k}_2 \cdot \vec{r}\,|_{x=0} = \vec{k}_3 \cdot \vec{r}\,|_{x=0} \tag{2.64}$$

$$\omega_1 \cdot t = \omega_2 \cdot t = \omega_3 \cdot t \tag{2.65}$$

Therefore, the angular frequency ω of the incident, transmitted and reflected wave is equal. At x=0, $\vec{r}$ is splitted up into its spacial parts. Using the dispersion relation (Equ. 2.54) leads to:

$$\vec{r} = y\hat{y} + z\hat{z} \tag{2.66}$$

$$\vec{k}_1 = n_1 \frac{\omega}{c} \left(k_{y_1}\hat{y} + k_{z_1}\hat{z} \right) \tag{2.67}$$

$$\vec{k}_2 = n_2 \frac{\omega}{c} \left(k_{y_2}\hat{y} + k_{z_2}\hat{z} \right) \tag{2.68}$$

$$\vec{k}_3 = n_1 \frac{\omega}{c} \left(k_{y_3}\hat{y} + k_{z_3}\hat{z} \right) \tag{2.69}$$

where $\hat{y}$ and $\hat{z}$ are the unit vectors of the axis y and z respectively. Using equation 2.64, the following equations are found:

$$k_{y_1} = k_{y_3} \tag{2.70}$$

$$k_{z_1} = k_{z_3} \tag{2.71}$$

$$k_{y_1} = \frac{n_2}{n_1} k_{y_2} \tag{2.72}$$

$$k_{z_1} = \frac{n_2}{n_1} k_{z_2} \tag{2.73}$$

Since the y-component of k_i is equal to $\cos(\alpha_i)$ and the z-component of k_i is equal to $\sin(\alpha_i)$, where i $= 1$ or 2, Snell's law is found [16]:

$$\alpha_1 = \alpha_2 \tag{2.74}$$

$$n_1 \cdot \sin(\alpha_1) = n_2 \cdot \sin(\alpha_2) \tag{2.75}$$
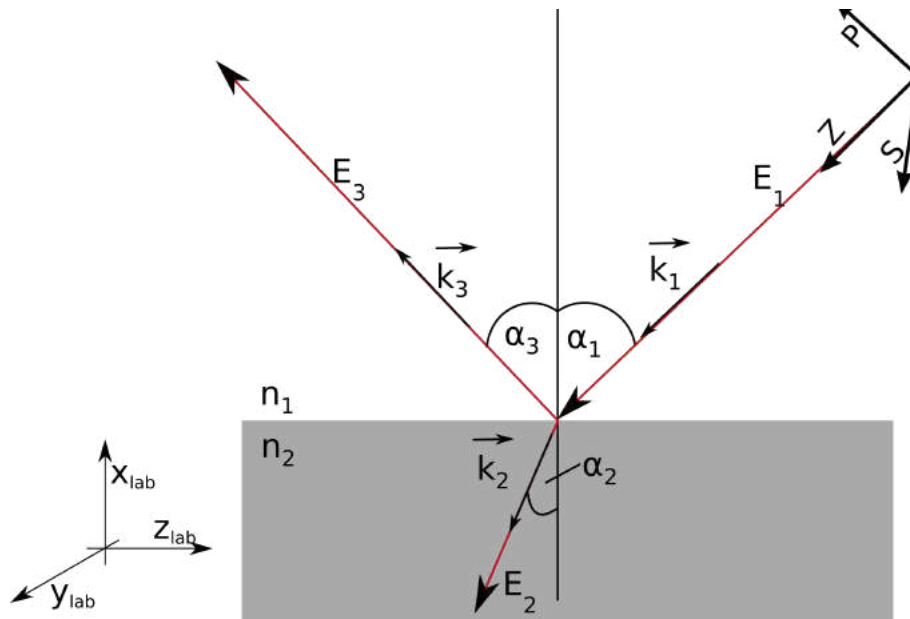

Figure 2.10: Sketch of an incoming ray, which is reflected and refracted according to Snell's law.

2.4.2 Intensity and Polarisation of Reflected and Refracted Light: Fresnel's Equations

The intensity of the reflected and refracted light in dependence of their polarisation direction is modelled by the Fresnel equations. Deriving these equations, again the model of an ideal dielectric (see Section 2.3.1) is used. Further, Maxwell's equations in integral form are used [16].

$$\int_S \epsilon \vec{E} \cdot d\vec{s} = \Delta Q \qquad\qquad \text{Gauss' law} \qquad (2.76)$$

$$\int_S \vec{B} \cdot d\vec{s} = 0 \qquad\qquad \text{Gauss' law for magnetism} \qquad (2.77)$$

$$\int_C \vec{E} \cdot d\vec{l} = -\int \frac{\partial \vec{B}}{dt} d\vec{s} \qquad\qquad \text{Faraday's law} \qquad (2.78)$$

$$\int_C \frac{\vec{B}}{\mu} \cdot d\vec{l} = \int_S \vec{J} \cdot d\vec{s} + \frac{\partial}{\partial t}\int_S \epsilon \vec{E} \cdot d\vec{s} \qquad\qquad \text{Ampère's law} \qquad (2.79)$$

When an electromagnetic wave propagates across an interface between two different materials, Maxwell's equations must hold [15, 16]. Based on this assumption, the boundary conditions, which constrain the behaviour of the electromagnetic wave at the interface, need to be calculated in order to derive Fresnel's equations.
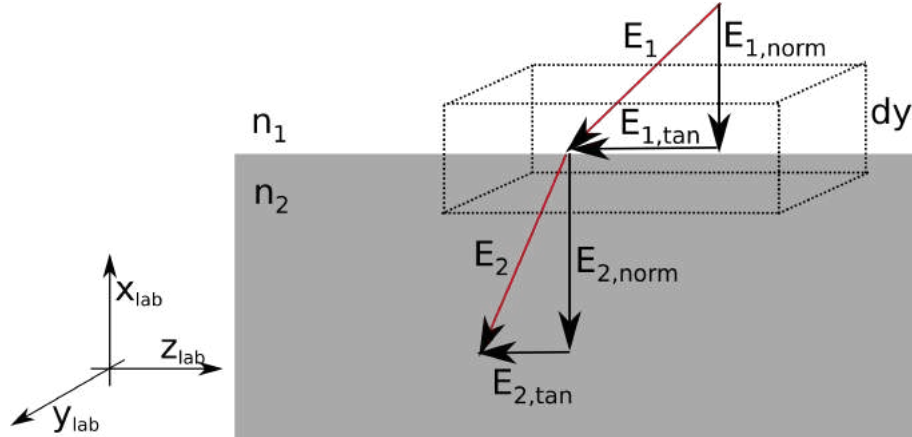

Figure 2.11: Sketch of the electric wave in material 1 with refractive index n_1 and material 2 with refractive index n_2 decomposed in a tangential component E_{tan} and normal component E_{norm}.

Therefore, the interfaces of two ideal dielectrics are examined. The electric wave $\vec{E}_1$ in medium 1 and the electric wave in medium 2 $\vec{E}_2$ are decomposed in a tangential component $\vec{E}_{tan}$ and normal component $\vec{E}_{norm}$ (see Figure 2.11). According to Gauss' law, the electric field is integrated over the area of an arbitrary volume, suggested in figure 2.11 by the dotted lines. Since Maxwell's equations must hold for any volume, we are not restricted to letting the height dy of the volume be infinitesimal [15]. Therefore, the volume is infinitesimal and the charge inside the volume ΔQ is zero. Further, only the area of the volume parallel to the surface has

an influence. Therefore, the first boundary condition is found to be:

$$\int_S \epsilon \vec{E} \cdot d\vec{s} = -\epsilon_1 \cdot E_{1,norm} + \epsilon_2 \cdot E_{2,norm} = 0 \tag{2.80}$$

$$\Rightarrow \epsilon_1 \cdot E_{1,norm} = \epsilon_2 \cdot E_{2,norm} \tag{2.81}$$

Performing the same calculations starting from Gauss' law for magnetism, the second boundary condition is found:

$$\int_S \vec{B} \cdot d\vec{s} = B_{1,norm} + B_{2,norm} = 0 \tag{2.82}$$

$$\Rightarrow B_{1,norm} = B_{2,norm} \tag{2.83}$$

In order to find the third boundary condition, Faraday's law is applied to the boundary. Therefore, a closed loop integral is performed, suggested in figure 2.12 by the dotted lines. Since the integral along the path l_2 and l_4 are equal except of an opposite sign, only the integrations along the path l_1 and l_3 have to be considered. Further, the normal component of the electric field has no effect to the integral along the path l_1 and l_3. However, Faraday's law must be true for every closed loop integral. Therefore, the path l_2 and l_4 are assumed to be infinitesimal and as a consequence, $d\vec{s}$ is zero. Thus, the right hand side of Faraday's law is zero and the boundary condition is found to be:

$$\int_C \vec{E} d\vec{l} = E_{1,tan} - E_{2,tan} = 0 \tag{2.84}$$

$$\Rightarrow E_{1,tan} = E_{2,tan} \tag{2.85}$$

Performing the same calculations starting from Ampères' law, the fourth boundary condition is found to be:

$$\int_C \frac{\vec{B}}{\mu} d\vec{l} = \frac{B_{1,tan}}{\mu_1} - \frac{B_{2,tan}}{\mu_2} = 0 \tag{2.86}$$

$$\Rightarrow \frac{B_{1,tan}}{\mu_1} = \frac{B_{2,tan}}{\mu_2} \tag{2.87}$$

As described in section 2.2, every electromagnetic wave can be decomposed into a P- and S-Polarised component (see Figure 2.13). In a dielectric, the electric and
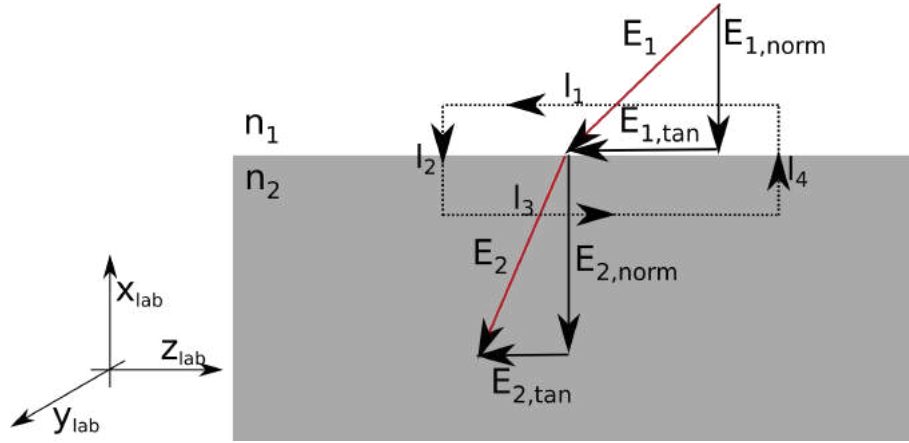
Figure 2.12: Sketch of the electric wave in material 1 with refractive index n_1 and material 2 with refractive index n_2 decomposed in a tangential component E_{tan} and normal component E_{norm}.

magnetic field behave not independently, but follow the conditions [5, 6]:

$$|B_P| = \frac{|E_S| \cdot \mathcal{N}}{c} \tag{2.88}$$

$$|B_S| = \frac{|E_P| \cdot \mathcal{N}}{c} \tag{2.89}$$

Having the four boundary conditions and the relations 2.88 and 2.89, the Fresnel's equations are found by investigating the P- and S-Polarisation at the boundary of material 1 and material 2.
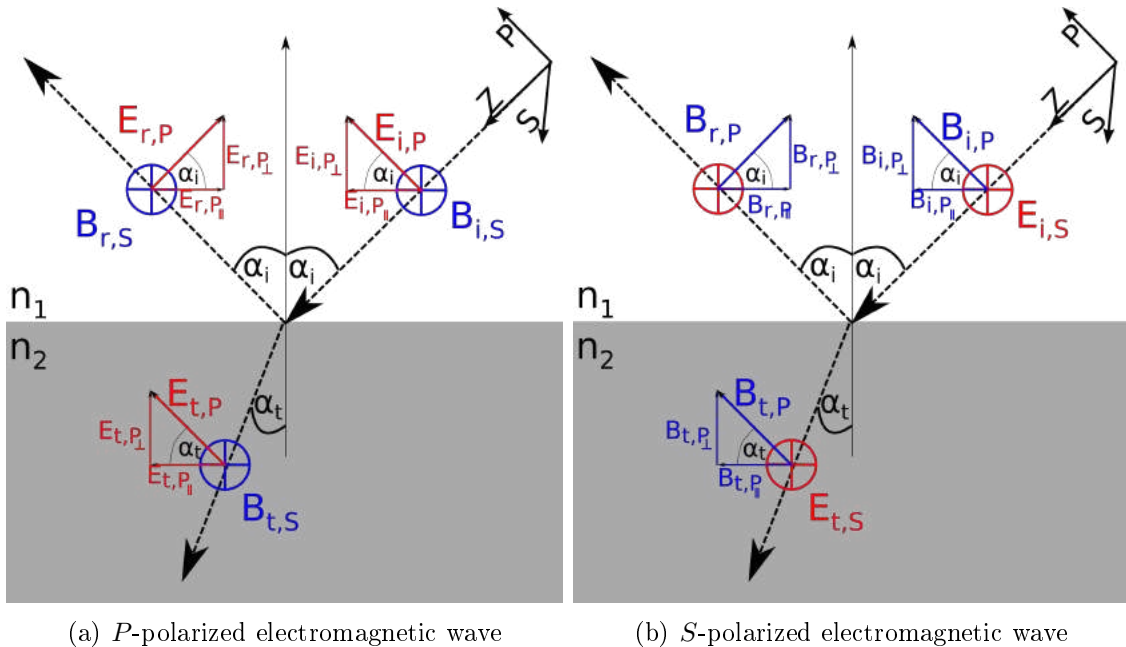
(a) P-polarized electromagnetic wave   (b) S-polarized electromagnetic wave

Figure 2.13: Sketch of an P- S-polarized electromagnetic wave reflected/transmitted at a boundary between two dielectrics. The electric field E (a) or the magnetic field (b) is decomposed into a parallel and perpendicular component in relation to the boundary surface.

P-Polarisation

For P-Polarised waves, the boundary conditions 2.87 and 2.85 are used. In the first boundary condition, $B_{1,S}$ is the sum of the perpendicular (denoted by S) component of the incident and reflected magnetic filed, where $B_{2,S}$ is the transmitted magnetic field.

$$B_{i,S} + B_{r,S} = B_{t,S} \tag{2.90}$$

$$\overset{2.89}{=} E_{i,P} \cdot \mathcal{N}_1 + E_{r,P} \cdot \mathcal{N}_1 = E_{t,P} \cdot \mathcal{N}_2 \tag{2.91}$$

Thence, the boundary condition 2.85 can be replaced by the parallel components (denoted by P) of the electric filed (see Figure 2.13 (a)):

$$E_{1,\parallel} = E_{2,\parallel} \tag{2.92}$$

$$= -E_{i,P} \cdot cos(\alpha_i) + E_{r,P} \cdot cos(\alpha_i) = -E_{t,P} \cdot cos(\alpha_t) \tag{2.93}$$

In combination with equation 2.91, the Fresnel's equations for P-Polarised light is found:

$$\overset{2.91}{=} \begin{cases} \dfrac{E_{r,P}}{E_{i,P}} = \dfrac{\mathcal{N}_2 \cdot \cos(\alpha_i) - \mathcal{N}_1 \cdot \cos(\alpha_2)}{\mathcal{N}_1 \cdot \cos(\alpha_t) + \mathcal{N}_2 \cdot \cos(\alpha_i)} = r_P \\ \dfrac{E_{t,P}}{E_{i,P}} = \dfrac{2 \cdot \mathcal{N}_1 \cdot \cos(\alpha_i)}{\mathcal{N}_1 \cdot \cos(\alpha_t) + \mathcal{N}_2 \cdot \cos(\alpha_i)} = t_P \end{cases} \tag{2.94}$$

S-Polarisation

For S-Polarised electromagnetic waves, the boundary conditions 2.81 and 2.83 are used. In the first boundary condition, $E_{1,S}$ is the sum of the incident and reflected electric field, where $E_{2,S}$ is the transmitted electric field:

$$E_{i,S} + E_{r,S} = E_{t,S} \tag{2.95}$$

The boundary condition 2.83 is replaced by the parallel components of the magnetic field (see Figure 2.13 (b)). Using equation 2.88, the Fresnel's equations for S-polarized light is found:

$$B_{1,\parallel} = B_{2,\parallel} \tag{2.96}$$

$$= -B_{i,\parallel} + B_{r,\parallel} = -B_{t,\parallel} \tag{2.97}$$

$$= -B_{i,P} \cdot \cos(\alpha_i) + B_{r,P} \cdot \cos(\alpha_i) = -B_{t,P} \cdot \cos(\alpha_t) \tag{2.98}$$

$$\overset{2.88}{=} -E_{i,S} \cdot \mathcal{N}_1 \cdot \cos(\alpha_i) + E_{r,S} \cdot \mathcal{N}_1 \cdot \cos(\alpha_i) = -E_{t,S} \cdot \mathcal{N}_2 \cdot \cos(\alpha_t) \tag{2.99}$$

$$\overset{2.95}{=} \begin{cases} \dfrac{E_{r,S}}{E_{i,S}} = \dfrac{\mathcal{N}_1 \cdot \cos(\alpha_i) - \mathcal{N}_2 \cdot \cos(\alpha_t)}{\mathcal{N}_1 \cdot \cos(\alpha_i) + \mathcal{N}_1 \cdot \cos(\alpha_t)} = r_S \\[3mm] \dfrac{E_{t,S}}{E_{i,S}} = \dfrac{2 \cdot \mathcal{N}_1 \cdot \cos(\alpha_i)}{\mathcal{N}_1 \cdot \cos(\alpha_i) + \mathcal{N}_2 \cdot \cos(\alpha_t)} = t_S \end{cases} \tag{2.100}$$

Equation 2.94 and 2.100 are the well known Fresnel's equations [16]. The absolute value of the reflection coefficients, $|r_S|^2$ and $|r_P|^2$, describes the intensity ratio of the incident and reflected beams. In this thesis, R is called reflectivity.

$$R_P = \frac{I_{r,P}}{I_{i,P}} = |r_P|^2 = \left| \frac{\mathcal{N}_2 \cdot \cos(\alpha_i) - \mathcal{N}_1 \cdot \cos(\alpha_t)}{\mathcal{N}_1 \cdot \cos(\alpha_t) + \mathcal{N}_2 \cdot \cos(\alpha_i)} \right|^2 \tag{2.101}$$

$$R_S = \frac{I_{r,S}}{I_{i,S}} = |r_S|^2 = \left| \frac{\mathcal{N}_1 \cdot \cos(\alpha_i) - \mathcal{N}_2 \cdot \cos(\alpha_t)}{\mathcal{N}_1 \cdot \cos(\alpha_i) + \mathcal{N}_2 \cdot \cos(\alpha_t)} \right|^2 \tag{2.102}$$

Since the angle of deflection is usually not known, it was replaced by Snell's law:

$$\alpha_t = sin^{-1}\left(\frac{n_1}{n_2}\right)\alpha_i \tag{2.103}$$

However, for any angle of incident, energy must be conserved. Therefore, for materials with negligible absorption, the following relation must hold:

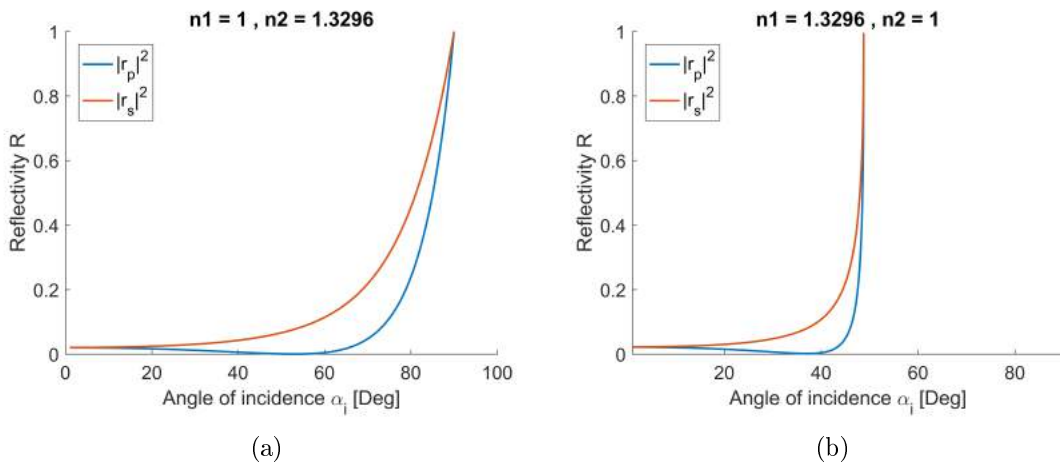$$T_P = 1 - R_P \tag{2.104}$$

$$T_S = 1 - R_S \tag{2.105}$$

$$\tag{2.106}$$

Figure 2.14: Fresnel reflection on a surface between air ($n_{air} = 1$) and water ($n_{water} = 1.3296$ at $\lambda = 785$nm). (a) Shows the transition form air to water for P- and S-Polarisation. On the other hand, (b) shows the transition form water to air. For angles larger than 48.77°, total internal reflection occures.

Figure 2.14 shows the Fresnel reflection on a surface between air ($n_{air} = 1$, $\kappa_{air} = 0$) and water ($n_{water} = 1.3296$, $\kappa_{water} = 0$, at $\lambda = 785$nm) according to equations 2.101 and 2.102.

Four special angles of incidents are noteworthy [17]:

Brewster angle α_B

At the Brewster angle, the P-Polarised incident beam is completely extinguished upon transmission. These angle can be calculated as follows:

$$\alpha_B = tan^{-1}\left(\frac{n_2}{n_1}\right) \tag{2.107}$$

The Brewster angle occurs both when light propagates across a surface from a material of lower refractive index to a material of higher refractive index and vice versa.

Critical angle α_C

The critical angle marks the upper limit of the angle of incident, where transmission occurs. For angles of incident higher than the critical angle, these phenomena is called total internal reflection and occurs only when light propagates across a surface form a material of higher refractive index to a material of lower refractive index and is calculated as follows:

$$\alpha_C = sin^{-1}\left(\frac{n_2}{n_1}\right) \tag{2.108}$$

Angle of incident of 45° and angle of incident, where the angle of refraction is 45°

At both, the angle of incident of 45° and the angle of incident, where the angle of refraction is 45°, the little known relation for the reflectivity of P- and S-Polarised light is given:

$$R_P = (R_S)^2 \tag{2.109}$$

However, a higher complex refractive index κ manifests in a higher reflectivity. Figure 2.15 shows plots for a sample with constant real part of the refractive index $n = 1.3296$ and varying complex part of the refractive index κ between 0 and 0.8.
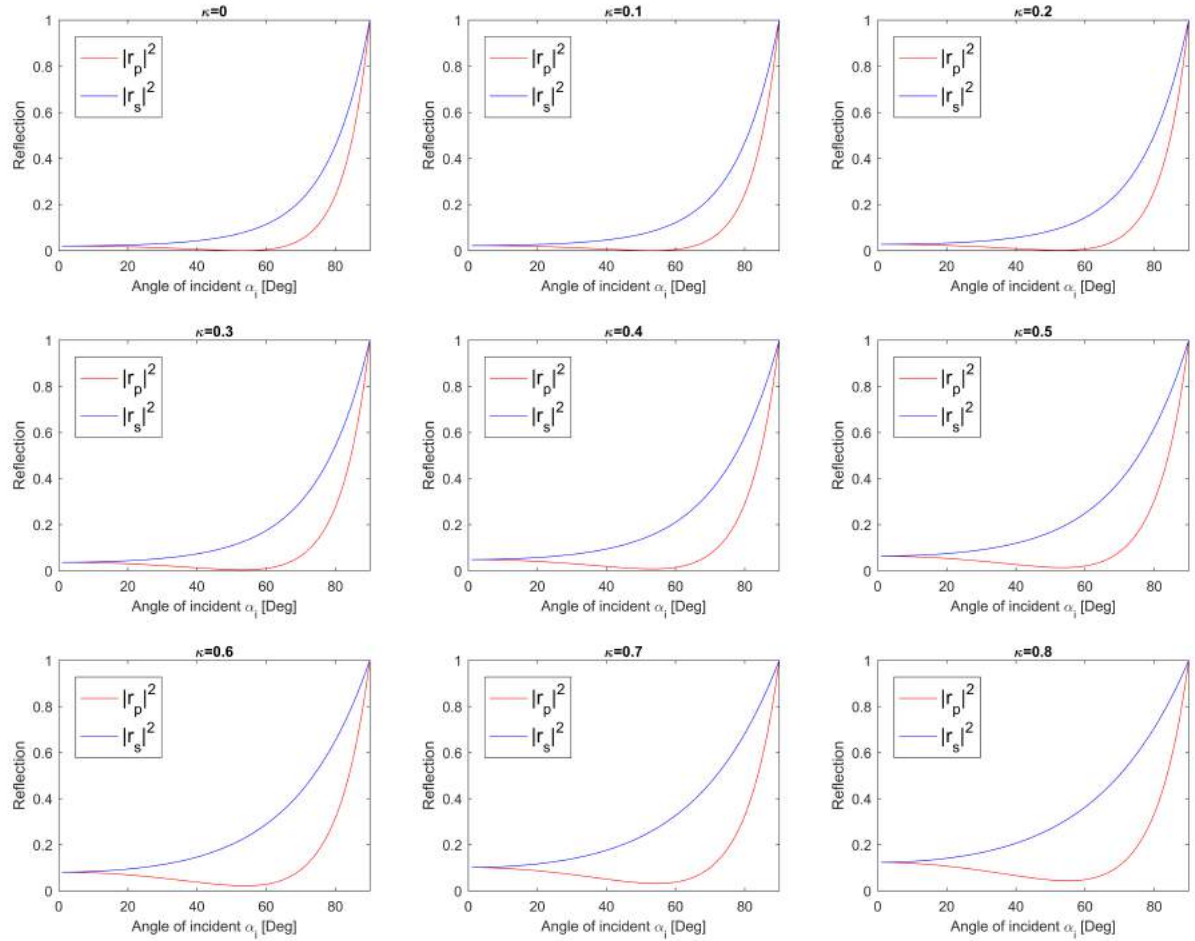

Figure 2.15: Influence of the complex refractive index to the reflectivity at a constant real part of the refractive index $n = 1.3296$.

2.4.3 Edwald-Oseen Extinction Theorem

When a incident beam propagates across a transition from media 1 with refractive index $\mathcal{N}_1$ to media 2 with refractive index $\mathcal{N}_2$, this incidence beam vanishes and is being replaced by two different beams, one propagating into the sample whereas one is reflected at the transition.

This extinction and creation of beams is not explained by the Fresnel equations (see Section 2.4.2). In contrast, the Ewald-Oseen extinction theorem resolves this paradox [18, 19]. Due to the linearity of Maxwell's equations, the total field at any point in space is expected to be the sum of the original (incident) field and the radiation produced by all the oscillating dipoles within the media. The Ewald-Oseen extinction theorem shows how the oscillation dipoles produce a field that cancels, by destructive interference, the original beam everywhere inside the the medium and results in a field which corresponds to that of the reflected and refracted beam. However, the proof of the Ewald-Oseen theorem is fairly straight forward, but involves complicated integrations over dipolar fields in three-dimensional space [20]. Thence, different approaches were developed on order to find a simple way to proof the Ewald-Oseen extinction theorem allow a physical insight [21, 22].

However, when investigating reflections, it is important to keep in mind that the reflection of a beam is influenced not only by the boundary but by the whole sample.

Chapter 3

Experimental Setup

3.1 Assets and Drawbacks of Transmission and Reflection Measurements

3.1.1 Transmission Measurements

A very common and often used device for measuring the real part of the refractive index n is the so called Abbe refractometer. This is a very precise and easy to use instrument [23, 24, 25] which is based on measuring the angle of refraction α_t (See Figure 2.10). With known angle of incidence α_i and refractive index n_1 of medium 1, Snell's law is applied to determine the unknown refractive index n_2 of the sample (see Equ. 2.75). However, the angle of refraction is usually read from a scale by eye. As a consequence, using an Abbe refractometer, the refractive index can only be determined in the visible range [25].

On the other hand, the sample has to be optically transparent in order to perform transmission measurements. Therefore, the sample needs to be prepared in as much as the incident beam propagates through the sample with neglecting extinction. This can be achieved by lowering the samples concentration of scattering/absorbing particles or by reducing the thickness of the sample. For biological tissues, this is often not possible without changing the tissue's optical parameters.

Also, since the incident beam needs to propagate through the sample, in vivo measurements are almost impossible using the Abbe refractometer.

3.1.2 Reflection Measurements

According to Fresnel's equations (Equ. 2.94 and 2.100), the intensity ratio of the incident beam $I_{i(P,S)}$ and the directly reflected beam $I_{r(P,S)}$ depend on the sample's complex refractive index $\mathcal{N}_2$. With known refractive index $\mathcal{N}_1$, angle of incidence α_1 and measured intensities of the incident and reflected beam, the sample's refractive index can be determined. Despite the simplicity of the Fresnel's equations, its

applicability to strongly scattering materials proves to be challenging.

The main part of the incident beam is transmitted into the sample and only a small fraction is directly reflected according to Fresnel's equations. In optically dense media, the transmitted light is backscattered diffusely. The directly reflected light is then overlaid on a background caused by diffusely backscattered light. As a consequence, the directly reflected light needs to be filtered out in order to apply Fresnel's equations.

However, the property of the surface needs to be taken into account when dealing with reflections. In general, two idealized types of reflections are distinguished: specular and Lambertian reflections. Specular reflections obeys Snell's law which states that an incident beam is reflected in a way that the angle of incidence is equal to the angle of refection. In contrast, diffuse reflection has an intensity distribution proportional to the cosine of the angle of reflection, called the Lambert's cosine law [26].
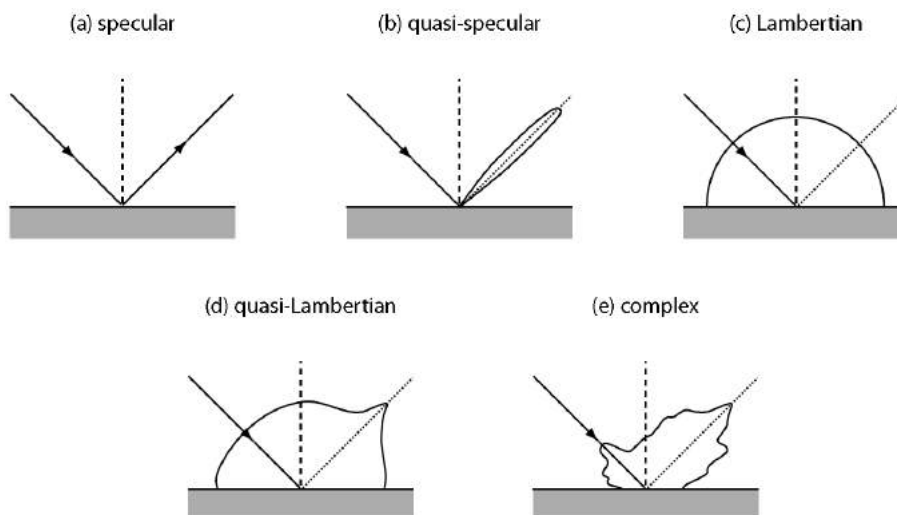

Figure 3.1: Schematic drawing of the different kind of reflections [27]

In order to distinguish which kind of reflection is dominant, the dimension of the surface roughness in comparison to the wavelength of the incident beam is decisive. When the surface roughness is larger than the wavelength of the incident beam, diffuse reflection is dominant whereas specular reflection dominates when the surface roughness is smaller than the wavelength [29]. However, the Fresnel equations deal only with specular reflections. Thence, applying Fresnel's equations to surfaces where the surface roughness is not negligible: either a correction term need to be added to these equations, or the experimental setup has to be built in a way that filters out the directly reflected beam.
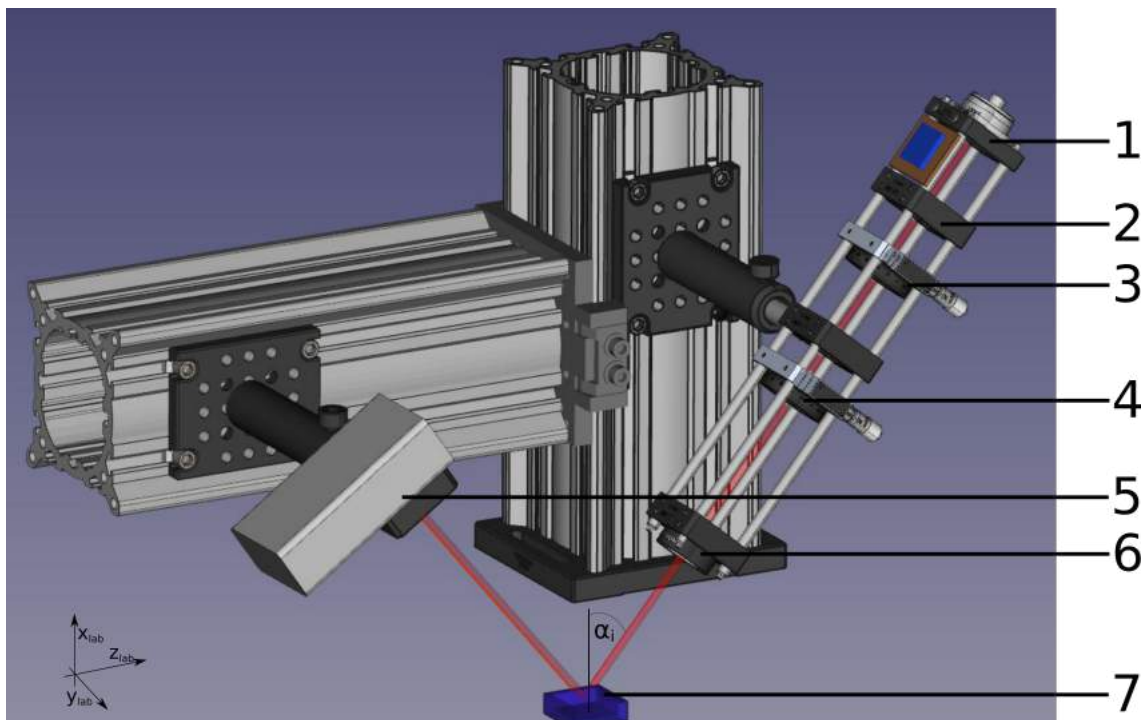
3.2 Experimental Setup

Figure 3.2: 3D model of the experimental setup. (1) Collimator, (2) 200 μm pinhole, (3) linear polariser, (4) half wave-plate, (5) CMOS imaging sensor, (6) neutral density filter, (7) sample under investigation

In order to be able to measure the refractive index of strongly scattering media, a setup was built based on reflection mode. A 3D model of this experimental setup is shown in figure 3.2. The sample under investigation is illuminated by a collimated Gaussian beam (Solea Supercontinuum Laser), passing a 200 μm pinhole, a linear polariser and a half wave-plate in order to rotate the illumination beam's polarisation state. The directly reflected and diffusely backscattered light was recorded as a two dimensional spacial distribution by a CMOS imaging sensor (PIXELINK PLA741, 320×240 px, $6.7 \mu m^2$/pixel). This imaging sensor was modified in as much as the protective glass in front of the sensor was removed to prevent interference effects from occurring. Further, a neutral density filter located at the end of the cage system prevented the CMOS chip from saturation. In order to achieve the best signal to noise ratio, the camera's exposure time was chosen individually for every recorded image in so that the highest pixel intensity was close to saturation. As a consequence, the linear increase of the intensity with increasing exposure time is an important requirement to the sensor. In order to verify this liner behaviour, the intensity was measured for different exposure times. As can be seen in figure 3.3, the detected intensity doubles with doubling exposure time up to an error in the order of 10^{-3}.
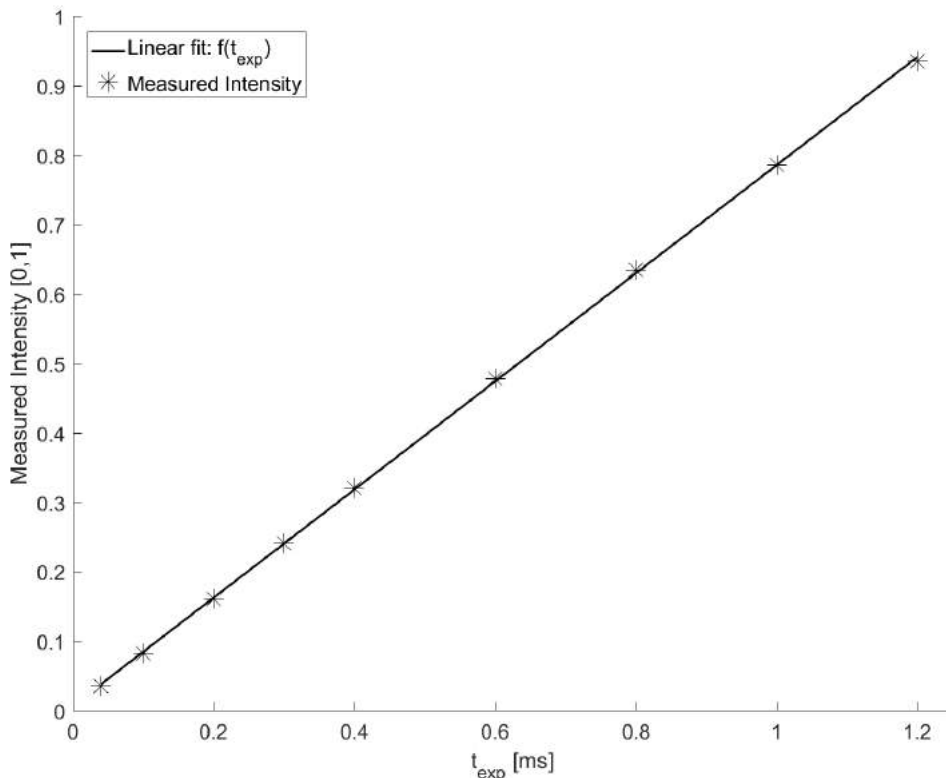
Figure 3.3: Intensity measurements at different exposure times performed with the PIXELINK CMOS detector. The linear fit reveals a small error in linearity. $f(t_{exp}) = 0.0069\pm0.0021 + (0.7786\pm0.0032)t_{exp}$

To determine the refractive index from a unknown sample with help of the Fresnel equations, not only the intensities of the incidence and reflected beams have to be measured, but also the angle of incident α_1. This was realized by a 3-axis accelerometer (LIS3DH, Adafruit Industries) with a 16 bit data output and a measurement range of ±2 g. The measured data were transmitted via I2C bus to an ATMega8 micro controller integrated on an Arduino board, where the processed data were read out with help of a commercial computer. The accelerometer was directly mounted on the setup's cage system and calibrated at 0° and 90° to the laboratory table, which was assumed to be perfectly horizontal.

Figure 3.4: Diagram of the data processing of the accelerometer (LIS3DH, Adafruit Industries). The measured data were sent via I2C-bus to a micro controller of type ATMega8 integrated on an Arduino board. The processed data were read out with a computer.

For the purpose of verifying the reliability of this angle measurements, two laser cut triangles, with an accuracy of $\pm 0.25°$ for each angle, were produced (see Figure 3.5).
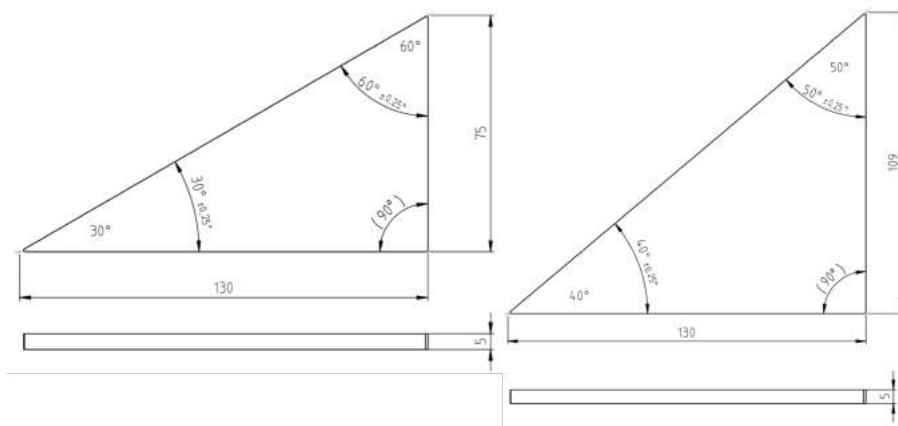

Figure 3.5: Laser cut triangles in order to verify the accelerometer's calibration. (Designed by Fabian Schuler, Gersag Krantechnik AG).
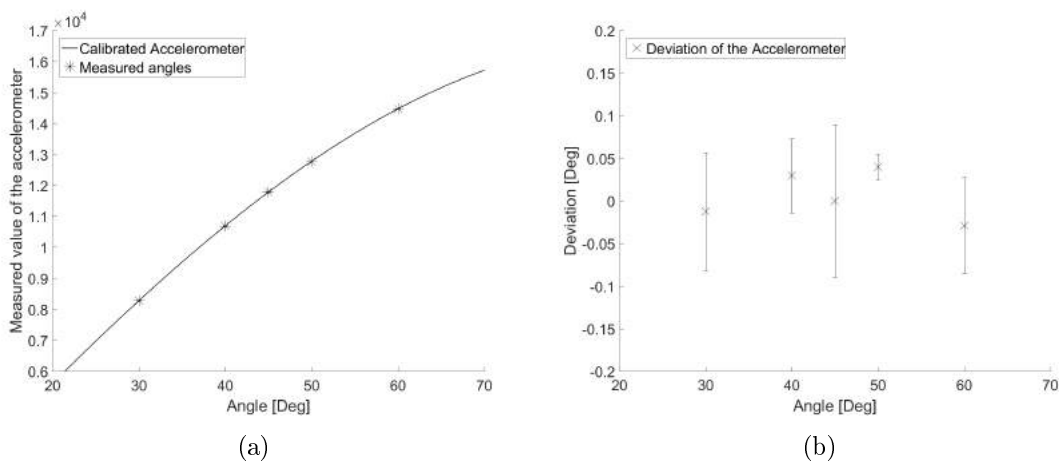

Figure 3.6: (a) Angle measurements with laser cut triangles in order to verify the calibration. (b) Absolute deviation of the measured angles compared to the laser cut triangles

The angle of incidence α_1 was then adjusted with help of the triangles and measured with the accelerometer. These measured angles can be found in figure 3.6 (a). The deviations of the accelerometer and the triangles can be found in 3.6 (b). For each angle, three measurements were performed. The errorbars represent the standard error.

However, not only the accelerometer has to be calibrated, but also the polarization state of the incident beam in order to achieve P- and S-Polarisation states. Therefore, the reflection of pure water was investigated by illuminating the water at the Brewster angle ($\alpha_B = 53.05°$ @ $\lambda = 785$nm). Then, the polarisation state of the incident beam was rotated until the intensity of the reflected beam vanished. The

so found polarisation state is then perfectly parallel to the plane of incidence, *i.e.*
P-Polarised. However, rotating the polarisation state of the incident beam around
90° (rotation of 45° of the wave-plate) results in a S-Polarisation state.

3.3 Error Estimation

Since the angle of incidence α_i, the reflectivity R and the polarisation state can
only be measured and adjusted in a limited precision, the effects on the measured
refractive index were investigated by Jones calculation (see Sec.2.2). For a given
sample with refractive index of water ($n = 1.3296$ @ $\lambda = 785\text{nm}$), the intensity of
the output state $|E_{out}\rangle$ was calculated for slightly various angles of incidence α and
polarisation states θ:

$$|E_{out}\rangle = \begin{pmatrix} -r_p & 0 \\ 0 & r_s \end{pmatrix} \begin{pmatrix} \cos(2\theta) & \sin(2\theta) \\ \sin(2\theta) & -\cos(2\theta) \end{pmatrix} \begin{pmatrix} \cos(\theta) \\ \sin(\theta) \end{pmatrix} |E_{in}\rangle \tag{3.1}$$

where θ is the polarisation angle relative to pure P-Polarisation, (r_p, r_s) the Fresnel
coefficients (see Equation 2.94 and 2.100) at the angle of incidence α_i, respectively.
However, in this estimation, the complex part of the refractive index was neglected.
From the so calculated intensity of the reflected field $I_r = ||E_{out}\rangle|^2$, the refractive
index was determined assuming an angle of incidence of 45° and a purely P-Polarised
illumination beam.

To investigate the effects inaccurate measurements of the illumination beams polari-
sation state, the reflectivity $R = I_r/I_i$ was calculated while changing the polarisation
angle θ from -1 ° to 1 °, where 0 ° means perfectly P-Polarised. With help of Fres-
nel's equations, the refractive index was calculated and can be found in Figure 3.7.
It can be seen that even for an incidence beam's polarisation state deviating from
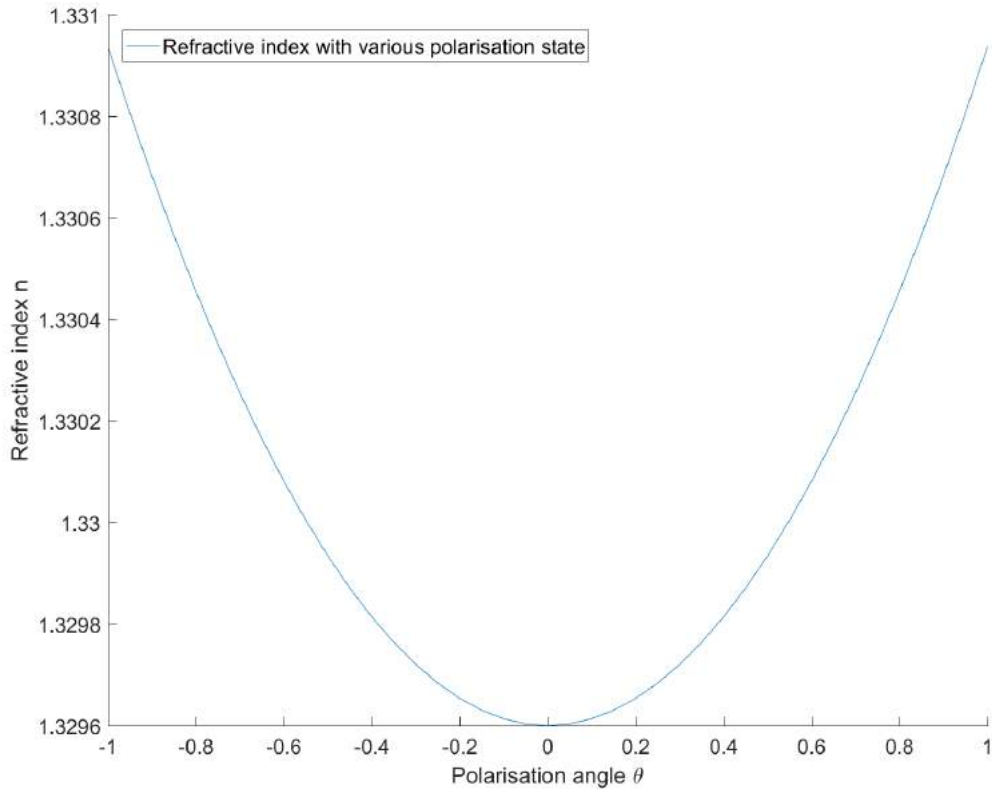the P-Polarisation state of $\pm 1°$, the change in the measured refractive index is small.

Figure 3.7: Measured refractive index in dependence of the polarisation state. At a constant angle of incidence of 45°, the refractive index was determined using Jones calculation while the polarisation state was changed.

To determine a sample's refractive index from Fresnel's equations, not only the incidence beam's polarisation state has to be well determined, but also the reflectivity $R = I_r/I_i$ and the angle of incidence. To investigate the effects on the determined refractive index for inaccuracies in the angle of incidence measurements, the reflectivity was calculated while changing the angle of incidence. The refractive index was then calculated form these reflectivity assuming an angle of incidence of 45°. Applying the same procedure for varying the calculated reflectivity, the effects on the refractive index for inaccuracies in the reflectivity measurements was investigated. Figure 3.8 shows the deviation from the input refractive index of $n = 1.3296$ with deviating angle of incident α_i and inaccuracies in the reflectivity measurements. The horizontal plane represents the input refractive index and serves as a reference. It can be seen that inaccuracies in the measured reflectivity R of $\pm 0.5\%$ results in a deviation of only about ± 0.001 for the refractive index. In contrast, the angle of incidence α_i has a big impact on the determined refractive index. An error for the angle of incidence of only 0.1° results in a deviation of the refractive index of nearly half a percent compared to the input value.
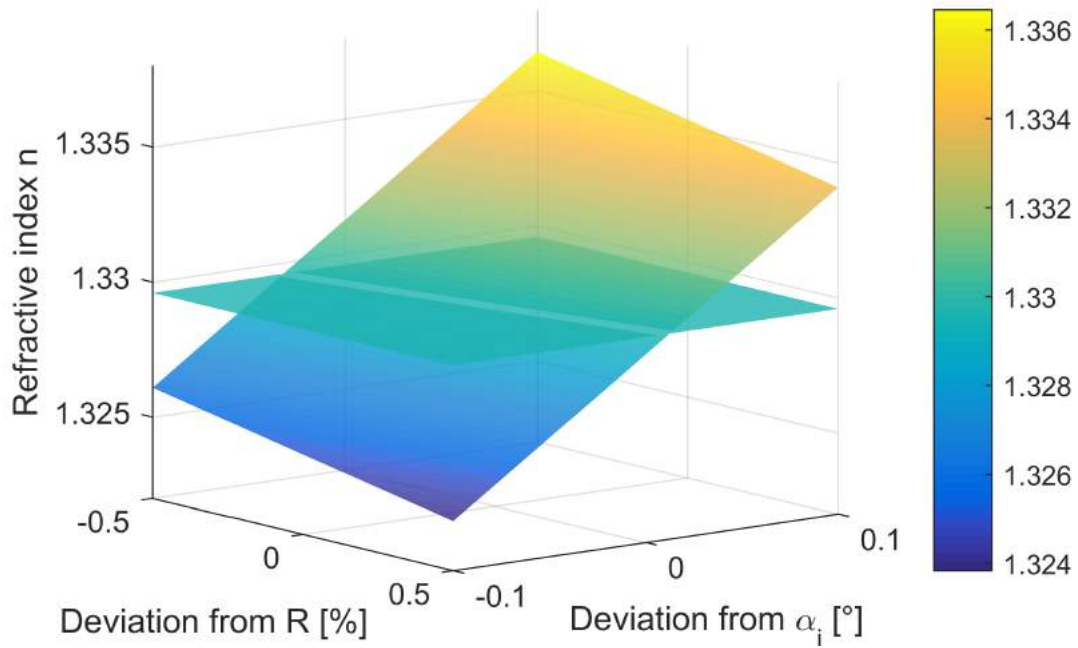
Figure 3.8: Measured refractive index in dependence of the angle of incidence and reflectivity. At a constant illumination beam's P-Polarisation state, the refractive index was determined using Jones calculation while varying the angle of incidence and reflectivity

However, with the here assumed deviations for the polarisation state, the reflectivity and angle of incidence measurements, the angle of incidence has the largest impact on the measured refractive index. As a consequence, in order to achieve precise refractive index measurements, the angle of incidence has to be measured very carefully.

3.4   Image Analysis

As mentioned in section 3.1, the directly reflected beam and diffusely backscattered light have to be unambiguously distinguished in order to determine the refractive index with Fresnel's equations. This is done by analysing the recorded images in two sequential steps, similar to what is explained in [30]:

- The first step consists in the analysis of the illumination beam, *i.e.* the determination of it's intensity. An image is recorded while replacing the sample by a mirror (Thorlabs Inc, BB3-E03). Then, a two-dimensional Gaussian function is fitted to the recorded intensity distribution in order to determine the illumination beam's intensity I_i.

$$I_{ill}(x,y) = I_i \exp\left(-\frac{(x-x_0)^2}{\sigma_x^2} - \frac{(y-y_0)^2}{\sigma_y^2}\right) \tag{3.2}$$

  where (x_0, y_0) are the profile's center points and (σ_x^2, σ_y^2) the variances of the Gaussian distribution.

- The second step consists in the analysis of the directly reflected beam from the sample.The sample is illuminated and an image of the directly reflected beam and the backscattered light is recorded. The assumption here is that the illumination beam being reflected according to Fresnel's equations, and therefore only the intensity but not the shape of the beam is changing.

$$I_{att}(x,y) = \alpha I_{ill}(x,y) + \text{background}(x,y) \tag{3.3}$$

  where $\alpha \leqslant 1$ is the factor, which expresses the attenuation of the illumination beam's maximum intensity. Since the detector's size is small compared to the solid angle, in which the light is backscattered (2π), the background's shape was assumed to be a curved surface second order.

$$\text{background}(x,y) = \beta_1(x-x_0)^2 + \beta_2(y-y_0)^2 \tag{3.4}$$
$$+ \beta_3(x-x_0) + \beta_4(y-y_0) + \beta_5 \tag{3.5}$$

(x_0, y_0) designates the coordinates of this surface's center point. The coefficients $\beta_{1..5}$ describe the bending and shape of the surface in the x- and y- directions. Hence, the maximum intensity I_r of $I_{att}(x,y)$ is given by: $I_r = \alpha I_i$.

Pure Water

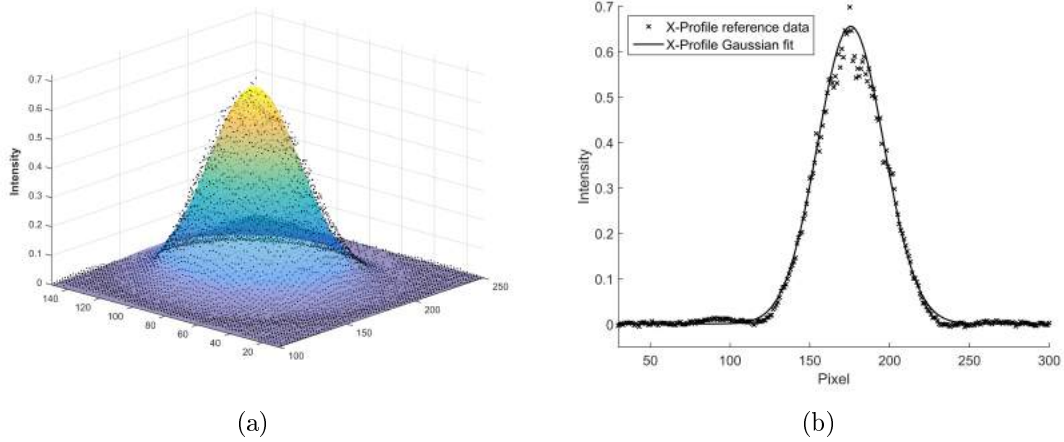<center>(a)</center> <center>(b)</center>

Figure 3.9: (a) 3D-Plot of the reference in order to determine the illuminating beam's intensity. The dots represent the intensity recorded by each pixel whereas the surface is the fitted Gaussian distribution. (b) X-Profile through the point of maximum intensity of the illuminating beam.

Figure 3.9 shows an example of a P-Polarized illuminating beam profile, reflected by a mirror replacing the sample at an angle of incidence of 45.05°. In sub figure (a), the intensity recorded by each pixel is represented by the dots. To this intensity distribution, a two dimensional Gaussian function is fitted (Equ. 3.2) in order to determine the illumination beam's intensity I_i. Sub figure (b) shows the X-Profile through the point of maximum intensity of the illumination beam. The recorded intensity of each pixel is represented by the crosses whereas the X-Profile of the fitted Gaussian function is showed by the solid line.

The determined intensity is I_i=0.6551±0.0049.

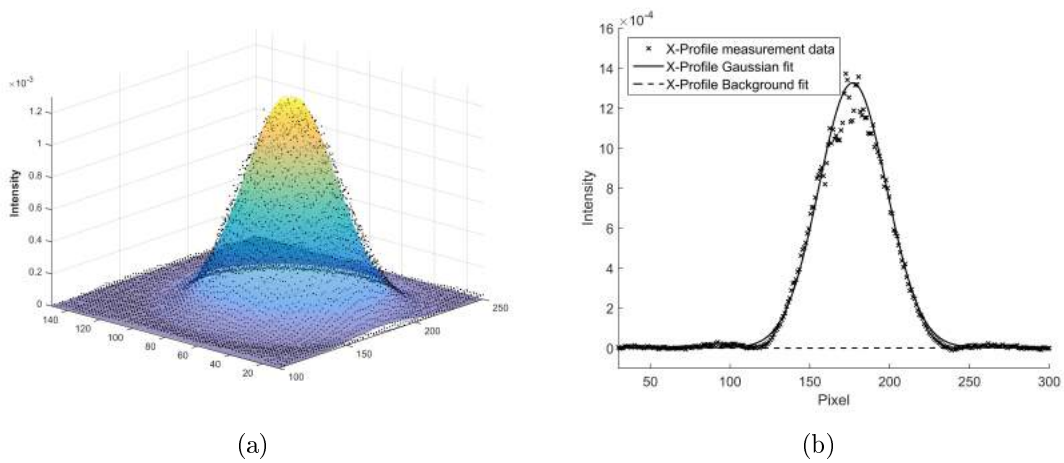<center>(a)</center> <center>(b)</center>

Figure 3.10: (a) 3D-Plot of the directly reflected beam of pure water in order to determine beam's intensity. The dots represent the intensity recorded by each pixel whereas the surface is the fitted Gaussian distribution. (b) X-Profile through the point of maximum intensity of the illuminating beam.

Figure 3.10 shows an example of a P-Polarized beam profile directly reflected by pure water at an angle of incidence of 45.05°. Since the samples mean free path $l^\star$ is large ($l^\star = 404.85$mm) [28], no background caused by backscattered photons is expected. To the recorded intensity distribution, a two dimensional Gaussian function (Equ. 3.4) is fitted in order to determine the intensity of the directly reflected beam I_r.
The determined intensity $\alpha = (2.696 \pm 0.0216) \cdot 10^{-3} \cdot I_i$

3.7% Latex suspension in H2O

Figure 3.11 and 4.1 show an example of the recorded image of the reference and directly reflected beam of a 3.7% latex suspension, respectively. The illuminating beam was in a P-Polarisation state at an angle of incidence of 45.05°. Due to the small mean free transport path ($l^\star = 0.0092$mm) in comparison to the sample's dimensions (length=56mm, width=36mm, height = 14mm), this latex suspension is strongly backscattering. Thence, the recorded beam profile is a superposition of the directly reflected beam and the background, caused by backscattering. In order to get the beam's intensity, the background was unambiguously filtered by fitting a background function to it (Equ. 3.4).

(a) (b)
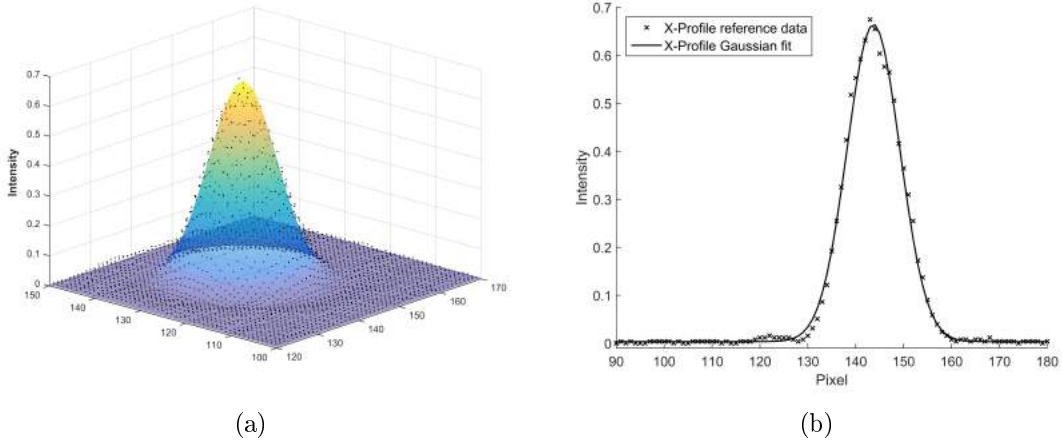
Figure 3.11: (a) 3D-Plot of the reference in order to determine the illuminating beam's intensity. The dots represent the intensity recorded by each pixel whereas the surface is the fitted Gaussian distribution. (b) X-Profile through the point of maximum intensity of the illuminating beam.

(a)   (b)

Figure 3.12: a) 3D-Plot of the directly reflected beam of a 3.7% latex suspension in pure water in order to determine beam's intensity. The dots represent the intensity recorded by each pixel whereas the surface is the fitted Gaussian distribution. (b) X-Profile through the point of maximum intensity of the illuminating beam.
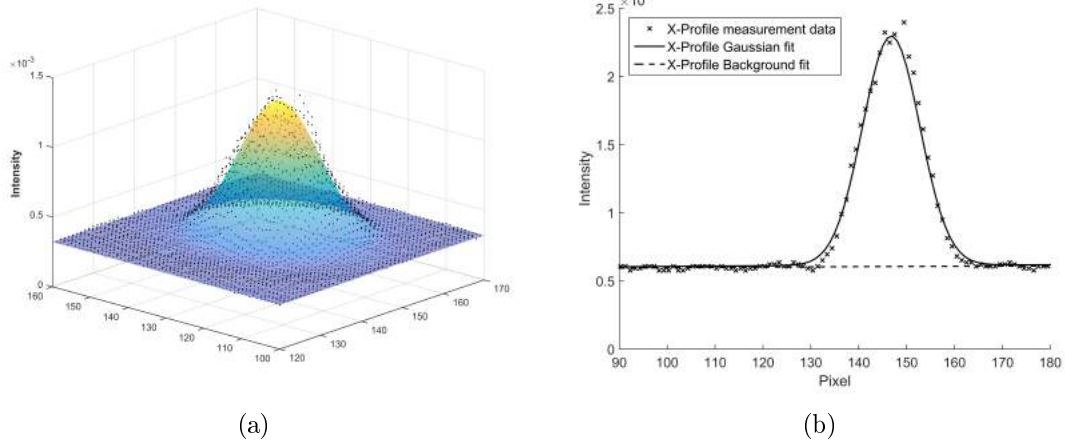
The determined intensities are: $I_i = 0.6613 \pm 0.0062$ and $\alpha = (2.780 \pm 0.0239) \cdot 10^{-3} \cdot I_i$.

Chapter 4

Setup Calibration and Measurement/Analysis Processes

Three different variations of the measurement and data analysis processes were investigated in order to develop a setup which allows expeditious and accurate measurements of the refractive index in strongly scattering media. In this Section, the samples under investigation were prepared in a way that surface roughness was negligible.

- In a first step, the procedure was based on measuring the intensity of the illumination and directly reflected beam as well as the angle of incidence. These data were then analysed with the help of the Fresnel's equations in order to determine the samples refractive index.

- The second step involves a different type of data analysis in order to be able to determine the refractive index independent of the illumination beam's intensity.

- In a third step, the measurement and data analysis were varied in as much as determining the refractive index independent of the illumination beam's intensity and angle of incident were possible.

In order to assess the accuracy of the setups, the refractive index of pure water and suspensions of latex spheres (Magsphere Inc, mean diameter of 350 nm, size parameter $\simeq$ 2.80) diluted in pure water was measured. The major advantage of latex spheres are the well known optical parameters. The real part of the refractive index for polystyrene latex (C8H8) is n=1.5788 at a wavelength of 785 nm and a temperature of 20° Celsius [31], whereas the complex part of the refractive index κ is negligible in comparison to that of water. However, at a wavelength of 785 nm, the water's complex refractive index is $\kappa = 1.5430 \cdot 10^{-7}$, what refers to an absorption

coefficient of μ_a=0.0247 cm^{-1} [32]. Thence, due to this absorption coefficient, the difference of the reflectivity for a sample without any absorption and a sample with an absorption coefficient of μ_a=0.0247 cm^{-1} is, according to Fresnel's equations, in the order of 10^{-14} for both, the P- and S-Polarisation. With this setup, it was not possible to measure the reflectivity with such a high precision. As a consequence, for all further samples, the complex refractive index was neglected.

However, the mean real part of the refractive index of a colloidal suspension was calculated according to the Avogadro-Biot-Beer-Landolt-Christiansen-Wintgen empirical law (ABBLCW-Law) [33] and served as a reference value.

## 4.1   Measurements in Dependence on the Illumination Intensity and Angle of Incidence

Applying Fresnel's equations is a common method in order to determine a sample's refractive index [3, 34, 35]. However, the sample's reflectivity and the angle of incidence need to be measured independently. In a first attempt, three suspensions of latex spheres diluted in pure water with volume fractions of 0%, 2.559% and 3.700% were investigated by measuring the reflectivity and the angle of incidence independently. The sample's mean free transport paths $l^\star$ were 404.85mm, 0.0132mm, 0.0092mm, respectively [28].

As described in Section 3.4, the illumination beam's intensity I_i was determined by recording and analysing an image while the sample was replaced by a mirror (Thorlabs Inc, BB3-E03). Further, the reflected beam of the sample under investigation was analysed in order to determine the directly reflected beam's intensity I_r. In addition, the angle of incidence α_i was measured by means of the accelerometer. However, inaccuracies in the measured angle of incidence α_i and the intensity measurements have a large impact on the accuracy of the determined refractive index (see Section 3.3). As a consequence, the sample's reflectivity was measured at multiple angles of incidence. These values were then fitted with Fresnel's equations (equ 2.101 and 2.102) in order to determine the sample's refractive index n.

(a) Pure Water
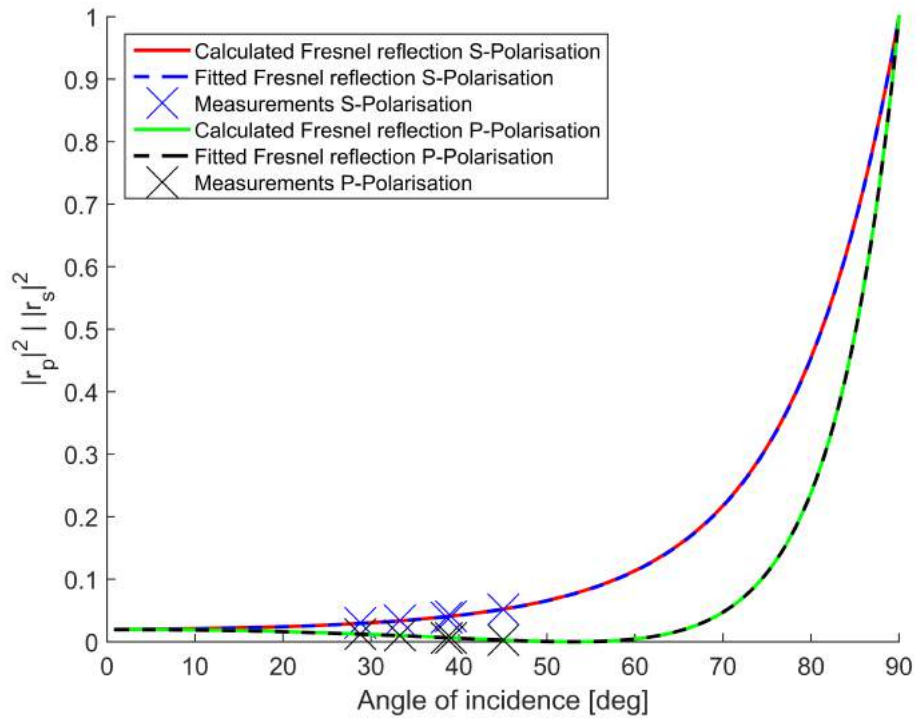
(b) 2.559% Latex Suspension
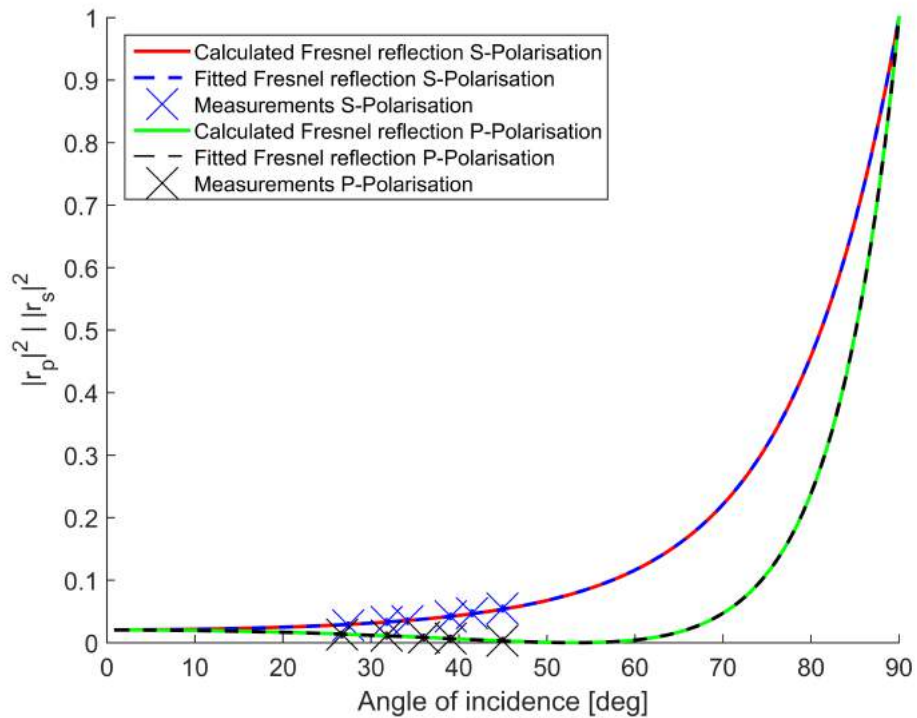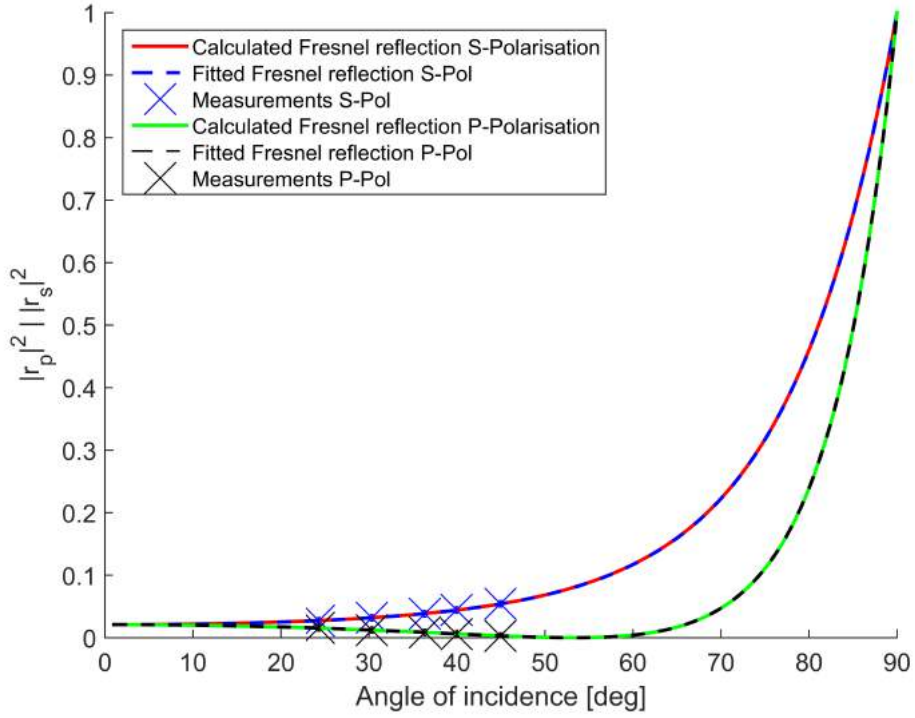
(c) 3.7% Latex Suspension

Figure 4.1: Measured intensity ratios of illumination and directly reflected beam of (a) pure water, (b) 2.599% and (c) 3.7% latex suspension, at different angles of incidence for P- and S-Polarisation. These values were, in order to determine the samples refractive index n, fitted with Fresnel equations

Sample	n_P	n_S	Literature [31, 32] ABBLCW-Law
Pure Water	1.3245±0.0026	1.3280±0.0024	1.3296
2.559% suspension	1.3338± 0.0042	1.3362± 0.0022	1.3359
3.7% suspension	1.3406±0.0091	1.3380±0.0012	1.3388

Table 4.1: Results of the determined refractive index at different latex volume fractions. The errors are the standard deviations from the least squared fit.

Table 4.1 shows the results of the determined refractive index for P- and S-Polarised incidence beams. The errors represent the standard deviation of the least square fit. It can be seen that the results are in good agreement with the calculated refractive index according to the ABBLCW-Law and reveal a deviation of only a few tenth of a percent.

However, it is noteworthy addressing some technical considerations to achieve accurate results. As the ratio of two independent acquisitions, I_i and I_r, need to be performed, a stable laser intensity during the measurement process is required. Further, the intensity of the illumination is recorded by replacing the sample by a mirror. On the one hand, the illumination beam is not perfectly collimated. Therefore, the reflection plane of the mirror needs to be located at exactly the same

position as the one of the sample. On the other hand, the reflectivity of the mirror needs to be 100%. In this setup, a mirror (Thorlabs Inc, BB3-E03) was used with a reflectivity close to 100% for angles of incidence $\alpha_i < 45°$ [36]. In contrast, for angles of incidence $\alpha_i > 45°$, the mirrors reflectivity was undetermined. Thence, the sample's reflectivity were measured only for angles of incident $\alpha_i < 45°$.

Further, in order to account for the camera's thermal noise, for each measurement step twenty images were recorded and averaged.

A difficulty occurs when the reflectivity of fluids is measured. As described in section 3.2, the angle of incidence α_1 is measured by means of an accelerometer which is calibrated relative to the laboratory table. However, when the sample is located in a small vessel, the fluids surface is bended due to surface tension (see Figure 4.2). As a consequence, the angle of incidence, measured by the accelerometer α_1, does not coincide with
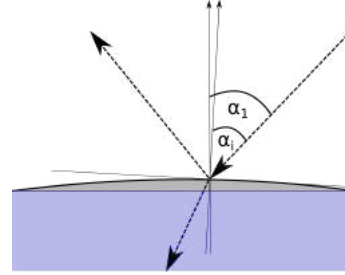
Figure 4.2: Sketch of the surface tension of a liquid sample when located in a small vessel. Consequently, the angle of incident (α_i) is not similar to the angle of incident measured with the accelerometer (α_1), which is calibrated to the horizontal aligned laboratory table.

the sample's angle of incidence defined by the surface's normal α_i. Thence, the vessel in which a liquid sample is located needs to be large enough, so that the surface's curvature due to surface tension is negligible.

Nevertheless, due to vibrations, surface waves can propagate over the fluid. These surfaces waves make the angle of incidence indeterminable. As a consequence, it has to be ensured that over the whole measurement process, vibrations, draughts or any effect that can generate surface waves are absent.

4.2 Measurements Independent of the Illumination Intensity

Applying Fresnel's equations in order to determine a sample's refractive index requires measurements of the illumination beam's intensity. As seen in Section 4.1 this intensity was measured by recording an image while the sample was replaced by a mirror. The reflectivity of this mirror was only definite for a limited angle of incidence of $\alpha_i < 45°$. As a consequence, precise measurements of the illumination beam's intensity were only possible within that limited range. In order to circumvent that issue, the analysis process modified in as much as refractive index measurements independent of the illumination beam's intensity were possible. The basic assumption behind that was that the intensity of the illumination beam at the two polarization states, namely P- and S-Polarization, was equal:

$$I_{i,P} = I_{i,S} \tag{4.1}$$

Since a half wave-plate was used to rotate the polarisation state of the illuminating beam, its intensity stayed constant. Using this equality of the intensities, the ratio of the reflected intensities for P- and S-Polarisation is a function of the angle of incidence α_i and the samples refractive index n_2.

$$\frac{R_S}{R_P} = \frac{\dfrac{I_{R,S}}{I_{i,S}}}{\dfrac{I_{R,P}}{I_{i,P}}} = \frac{I_{R_S}}{I_{R_P}} = \frac{\left| \dfrac{n_1 \cdot \cos(\alpha_i) - n_2 \cdot \cos(\alpha_t)}{n_1 \cdot \cos(\alpha_i) + n_1 \cdot \cos(\alpha_t)} \right|^2}{\left| \dfrac{n_2 \cdot \cos(\alpha_i) - n_1 \cdot \cos(\alpha_t)}{n_1 \cdot \cos(\alpha_t) + n_1 \cdot \cos(\alpha_i)} \right|^2} \tag{4.2}$$

where α_t is according to Snell's law

$$\alpha_t = sin^{-1}\left(\frac{n_1}{n_2}\right)\alpha_i \tag{4.3}$$

However, a problem occurs when recording the images with a CMOS detector for P- and S-Polarization. Since there are optical elements implemented in the camera, the detection sensitivity of the full system was different for P- and S-Polarisation. Therefore, equation 4.2 needs to account for that sensitivity factor, called γ:

$$\frac{I_{R_S} \cdot \gamma}{I_{R_P}} = \frac{\left| \dfrac{n_1 \cdot \cos(\alpha_i) - n_2 \cdot \cos(\alpha_t)}{n_1 \cdot \cos(\alpha_i) + n_1 \cdot \cos(\alpha_t)} \right|^2 by}{\left| \dfrac{n_2 \cdot \cos(\alpha_i) - n_1 \cdot \cos(\alpha_t)}{n_1 \cdot \cos(\alpha_t) + n_1 \cdot \cos(\alpha_i)} \right|^2} \tag{4.4}$$

For a beam entering the camera at normal incidence, the sensitivity factor was $I_S/I_P = 0.89$. In order to asses the effectivity of this analysis method, the refractive

index of a 2.599% latex suspension at a wavelength of 785 nm was determined by
measuring the ratio of the reflected intensities for P- and S-Polarisation at different
angles of incidence. For every angle of incidence, the reflectivity was measured ten
times. The The averaged measurements are shown in figure 4.3, represented by the
crosses where the standard deviations are shown by the errorbars.
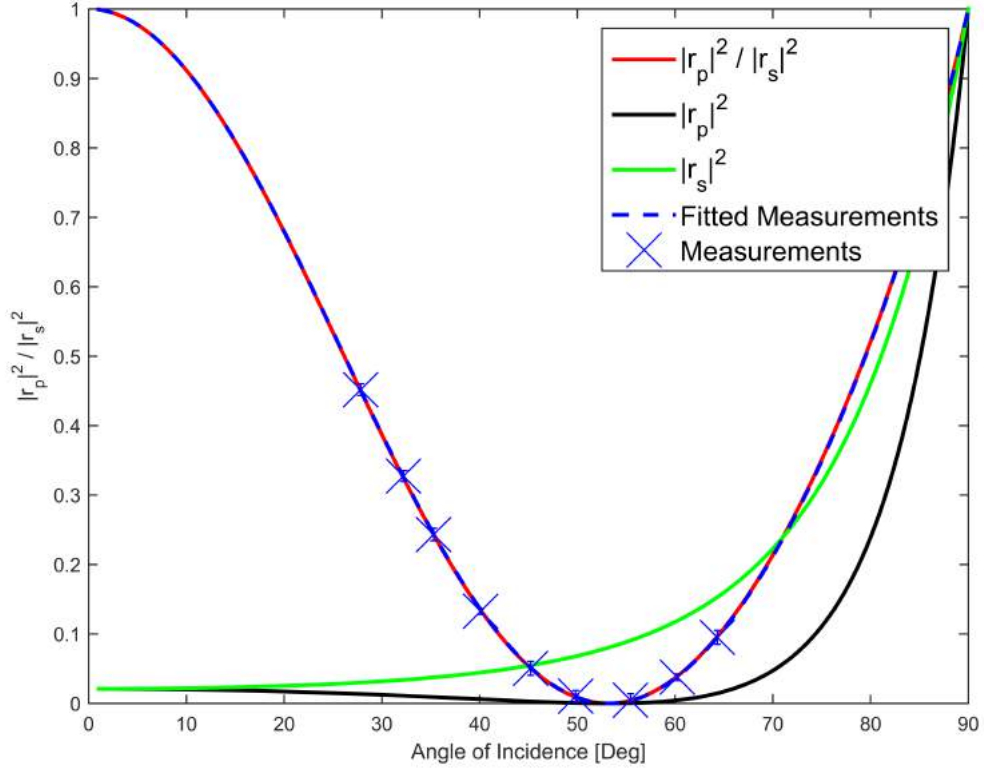
2.559% Latex Suspension

Figure 4.3: Measured intensity ratios of directly reflected P- and S-Polarised beams for 2.599%
latex suspension measured at different angles of incidence. These values were, in order to determine
the samples refractive index n, fitted with equation 4.4.

Sample	n	Literature [31, 32] ABBLCW-Law
2.559% suspension	1.3389±0.0041	1.3359

Table 4.2: Result of the determined refractive index. The errors are the standard deviations from
the least squared fit.

The results were fitted with equation 4.4 in order to determine the samples refractive
index. The so found refractive index is shown in table 4.2. The error represent the
standard deviation of the least square fit. It can be seen that the result is in good
agreement with the calculated refractive index according to the ABBLCW-Law and
reveal a deviation of only a few tenth of a percent.

However, the sensitivity factor γ highly depends the angle on which the beam enters

the camera system. When changing the sample's angle of incidence, the camera had to be repositioned in order to record the beam reflected by the sample. However, due to this modification, it can not be totally ensured that the angle with which the beam enters the camera system and the sensitivity factor γ stayed unchanged. Although change of the sensitivity factor after a setup modification was within the range of ± 0.02, the error on the determined refractive index when neglecting this change is in the order of nearly half a percent. Thence, the sensitivity factor γ was calibrated after every modification of the setup. As a consequence, determining the refractive index by analysing the reflected intensities for P- and S-Polarisation is only reasonable when a detection system is used where the sensitivity does not change for different polarisations.

4.3 Refractive Index Measurements Independent of both the Illumination Intensity and Angle of Incidence

The goal of this thesis was to develop a setup for measuring the refractive index of a unknown sample quickly and accurate with the purpose of the ability to perform scanning. Both, setup 1 and setup 2 result in accurate measurements. Nevertheless, in order to receive reliable results, the reflectivity was measured at multiple angles of incidence. This procedure is very time-consuming since the setup needs to be modified during the measurement process. Further, measuring the angle of incidence using an accelerometer turned out to be very delicate. On the one hand, since the accelerometer is mounted on the cage system, the beam needs to propagate perfectly perpendicularly to the cage system in order to determine the angle of incidence α_i properly. Thence, when modifying the setup in order to change the angle of incidence, it has to be ensured that the propagation direction of the beam had not changed accidentally. On the other hand, the accelerometer was calibrated in relation to the laboratory table. Thence, a sample's surface need to be aligned perfectly parallel to the laboratory table. This turned out to be challenging when investigating fluids since surface tension and vibrations change the fluid's surface alignment.

As a consequence, the setup was modified in as much as the refractive index can be determined without direct measurements of the angle of incident and the intensity of the illumination beam.

The unknown values in equation 4.2 are the intensity of the P- and S-Polarised incident beams, $I_{i,P}$ and $I_{i,S}$, the angle of incidence α_i and the refractive index of the sample n_2. In order to determine these four unknowns, at least four independent equations are needed.

Consequently, four independent values are need to be measured.

A straightforward approach is to cover the sample with plane glass of known refractive index in order to receive two reflections for each polarisation state. The first reflection occurs at the interface of air and glass (R_{1-2}) where the corresponding intensity of this reflected beam is measured directly at the detector (I_{R_1}). The part of the illuminating beam which entered the glass is reflected by the transition of glass and sample (R_{1-2}) and results in the intensity I_{R2} at the detector. Recording these two reflections for the P- and S-Polarisation, these four independent measurements determine the four unknowns α_i, $I_{i,P}$, $I_{i,S}$ and n_2. The modified setup, where the sample is covered with a plane glass plate of known refractive index is shown in figure 4.4.
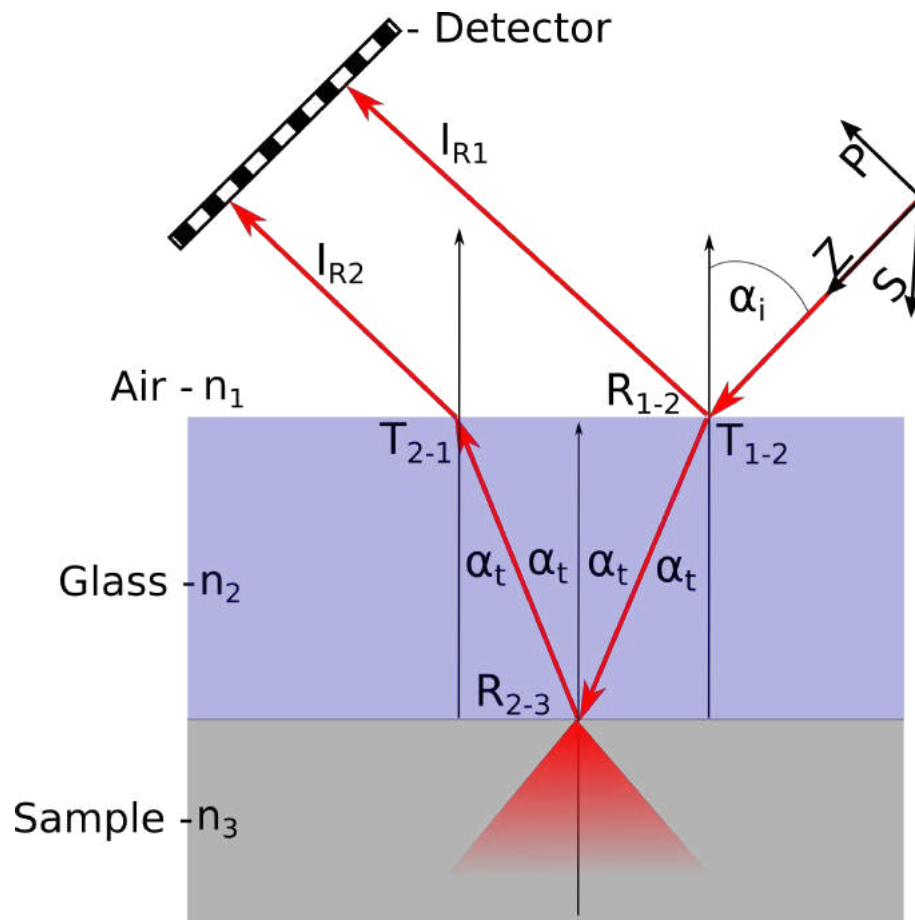

Figure 4.4: Sketch of the modified measurement procedure in order to measure the refractive index independent of the angle of incidence and the illumination beam's intensity.

The governing equations for determining the four unknowns ($I_{i,S}$,$I_{i,P}$,α_i,n_3) are the
following:

$$I_{R1_S} = I_{i,S} \cdot R_S\left(n_1, n_2, \alpha_i\right) \tag{4.5}$$

$$I_{R1_P} = I_{i,P} \cdot R_P\left(n_1, n_2, \alpha_i\right) \tag{4.6}$$

$$I_{R2_S} = I_{i,S} \cdot T_S\left(n_1, n_2, \alpha_i\right) \cdot R_S\left(n_2, n_3, \alpha_t\right) \cdot T_S\left(n_2, n_1, \alpha_t\right) \tag{4.7}$$

$$I_{R2_P} = I_{i,P} \cdot T_P\left(n_1, n_2, \alpha_i\right) \cdot R_P\left(n_2, n_3, \alpha_t\right) \cdot T_P\left(n_2, n_1, \alpha_t\right) \tag{4.8}$$

where R_S, R_P, T_S and T_P are the Fresnel equations. The angle of transmittance α_t
was replaced by Snell's law. Since the covering glass (BK7) had a thickness of only
10 mm, its absorption ($\mu_a = 0.14752$ m^{-1} [37]) was neglected.

Again, the method was examined by measuring the refractive index of latex suspen-
sions of different volume fractions. For each sample, at a fixed angle of incidence,
an image for each polarisation state containing the two reflections I_{R1} and I_{R2} was
recorded. These profiles were fitted by a Gaussian function in order to determine
their intensities I_{R1_S}, I_{R1_P}, I_{R2_S}, I_{R2_P}. The determined intensities were then used to
solve the system of equations 4.6 - 4.8 numerically. The solutions for the refractive
index n and the angle of incidence α_i are plotted in figure 4.5. For every sample,
five different measurements were performed and analysed. The errorbars in figure
4.5 correspond to their standard deviations.

The measurements of the refractive index are in good agreement with the ABBLCW-
Law and have a deviation of only a few tenth of a percent over the whole concen-
tration range.

Nevertheless, a closer look at the angle of incidence determined by solving the sys-
tem of equations reveals a variation for every concentration. However, in order to
replace the sample, the covering glass and the vessel were removed and cleaned.
After refilling the vessel with a new sample, the covering glass was remounted on
the vessel. Due to these modifications, the angle of incidence was changing for the
different samples. However, in order to verify that the refractive index measure-
ments are independent of the angle of incidence, for the samples of volume fraction
between 0.101% and 0.5%, the angle of incidence was slightly reduced.

This setup turned out to be able to determine the refractive index of a sample with-
out direct measurements of the angle of incidence and the illumination intensity.
Moreover, the same precision in measuring the refractive index compared to the
measurement where the angle of incidence was measured by means of an accelerom-
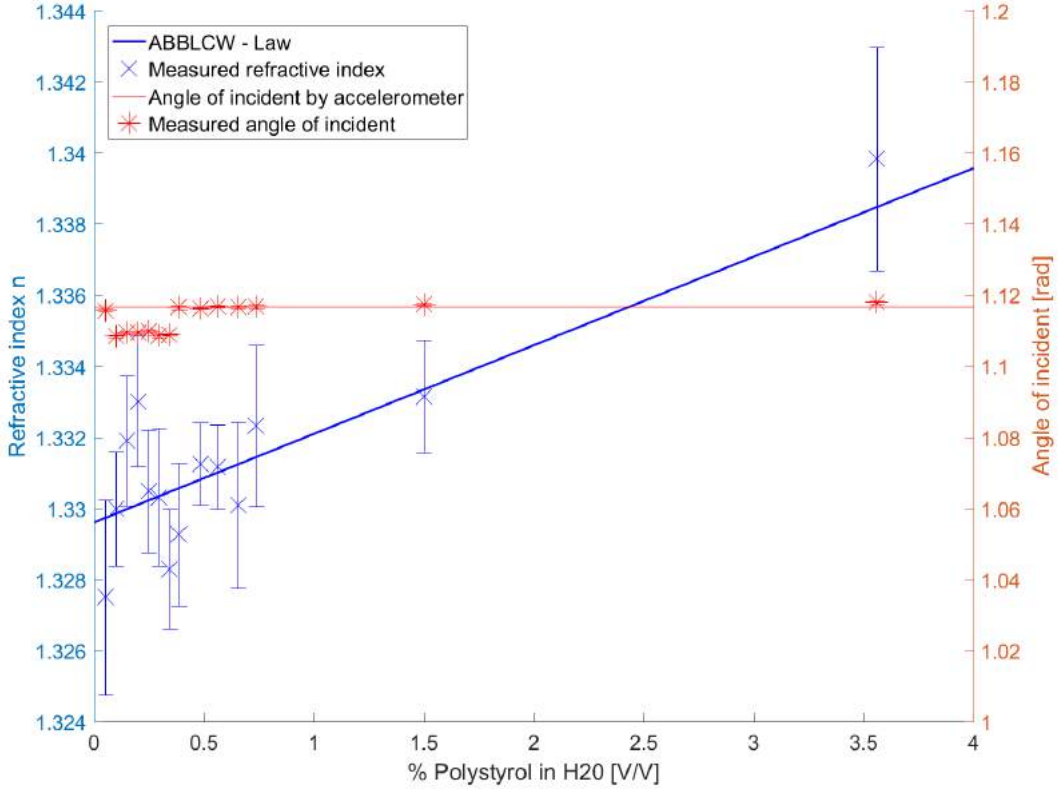eter could be achieved by performing only a single measurement at one angle.

Figure 4.5: Measured refractive index and angle of incident for different sample concentrations

4.3.1   Gelatin

In order to develop minimally invasive diagnostic tools, so-called "phantoms", which mimic human tissue, are used for a number of purposes *e.g.* testing the system, optimizing signal to noise ratio, performing quality control, comparing quality control between systems [38]. However, the optical properties of the phantom need to be well known in order to conduct light propagation experiments in a relevant manner. Therefore, the refractive index of a particular type of phantom, namely the gelatin phantom used in the framework of optoacoustic, was determined. The used gelatin sample contained 15.6% weight percentage of gelatin. In order to receive a reference value for the refractive index, a slice of the sample was investigated by means of an Abbe refractometer (ATAGO Type 1T) which is able to measure the refractive index only at the sodium d-line ($\lambda_D = 589.29$nm). The refractibe index measurements with help of the Abbe refractometer was performed 5 times and the mean value with its standard deviation can be found in table 4.3.

In order to measure the refractive index of the gelatin sample with the developed imaging setup described above, the gelatin sample was covered with a glass (BK7). In contrast to fluids, the gelatin sample does not have a plane surface. In order to still make good contact to the covering glass, the gelatin sample was squeezed in

between of two glasses. As pressure can change the optical properties of the sample, it is important to apply as low pressure as possible.

Wavelength [nm]	n_{Abbe}	$n_{Imaging}$
589.29	1.343	1.3393 ± 0.0014

Table 4.3: Result of the determined refractive index of a gelatin sample. For every wavelength, five measurements were performed. The errors represent the standard deviations

4.3.2   Salami

The developed setup is able to expeditiously and accurately measure the refractive index of a sample without being modified, *i.e.* changing the angle of incidence. Therefore, a sample composed of different tissue types can be scanned in order to determine the different regions of refractive indices. In a first approach, a one dimensional scan of commercial slice of salami was performed. One slice of salami is composed of meat with fat accumulation having a different refractive index than the enclosure meat. Therefore, when measuring the sample's refractive index over a certain distance, a deviation in the refractive index is expected due to the different tissue types.
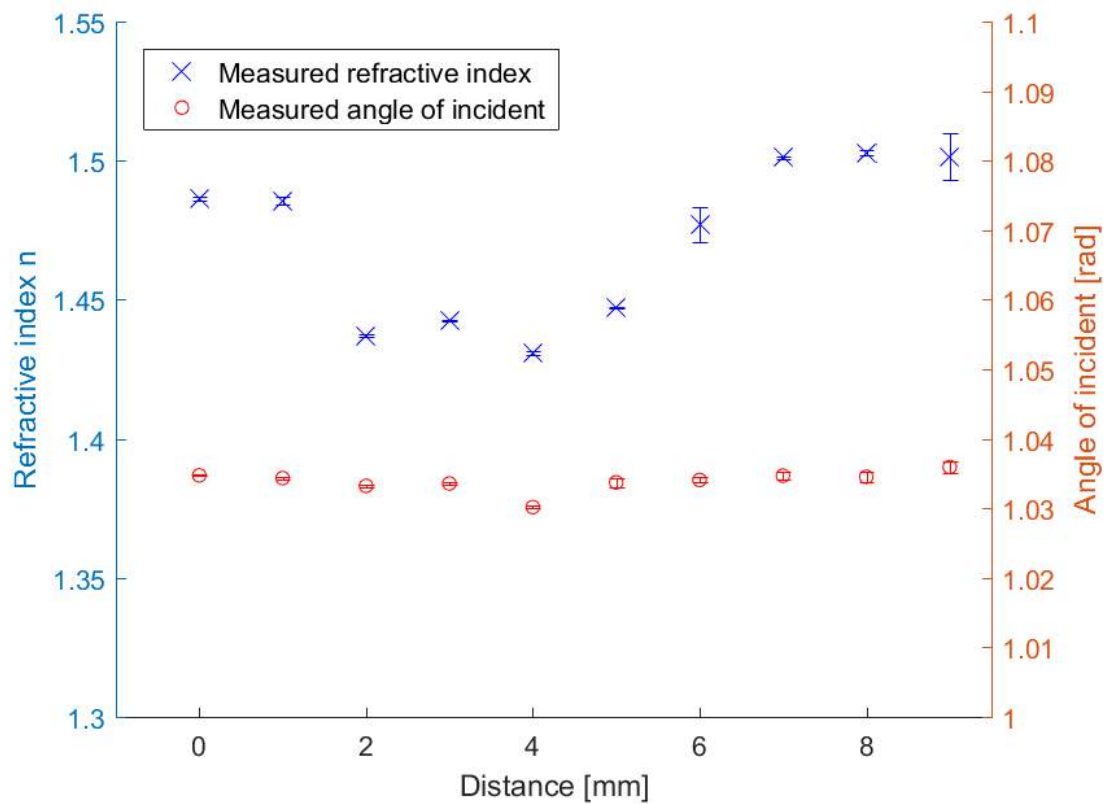

Figure 4.6: Measured refractive index and angle of incident for different locations at the slice of salami.

Figure 4.6 shows the scanned refractive indices and angles of incidence. The measurements were performed with 1 mm steps from the starting point (Figure 4.7 left green dot). By comparing the plot 4.6 and the image 4.7, it can be seen that the fat accumulation has a refractive index of about 1.48 whereas the meat has an refractive index of about 1.44. However, for positions located between 2 mm and 6 mm, the sample's meat is traversed by fat.

Figure 4.7: Image of the scanned slice of salami. The green dots represent the locations of measurements.

Therefore, not only the reflection of pure meat but also the reflection of fat is measured. Since the fraction of fat and meat within this region is not constant, the refractive index varies over this distance. Nevertheless, figure 4.6 reveals that there is a clear difference in refractive index for the different compounds of the salami.

Chapter 5

Accounting for Surface Roughness: Diffuse-Specular Reflections

5.1 Measurement and Analysis Principle

In the previous Chapter, only samples with plane surfaces, or samples where the surface was flatten, were investigated. Nevertheless, *e.g* the surface of human skin is highly uneven (see Figure 5.1) and therefore, a diffuse specular reflection is expected. However, filtering the directly reflected beam for diffuse specular reflections in order to apply Fresnel's equations is a difficult task. To receive specular reflection despite surface roughness, the method of covering the sample with a glass plate was investigated for samples without negligible surface roughness.

Since skin is composed of different layers containing microscopic cells, blood vessels etc. of different refractive indices, applying pressure in order to press the skin against a covering glass will change the refractive index of the skin [3, 34]. Therefore, reducing the surface roughness by squeezing the skin between two glass plates results in non-reliable measurements.
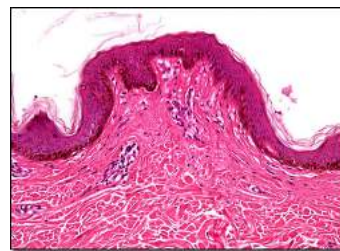

Figure 5.1: Microscopic image of a skin surface. It is clearly visible that the surface of the skin is highly uneven and therefore a diffuse specular reflection is expected [39].

In contrast, putting a covering glass on top of the sample without applying pressure results in areas in which the sample is in direct contact with the glass, whereas some air enclosure will prevent the sample from directly touch the glass. When illuminating the sample with a beam whose diameter is larger than the dimension of these air enclosures, the reflection which occurs at the transition from glass to skin (R_{2-3}) is a superposition of the reflection from the transition of glass-air and glass-skin (see Figure 5.2).
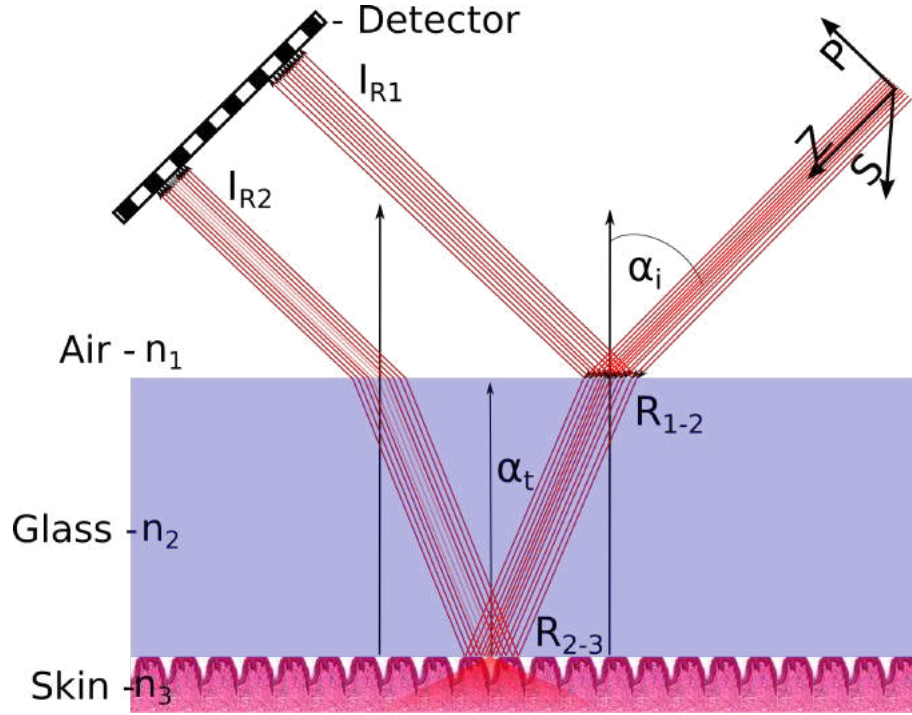
Figure 5.2: Sketch of a samples reflection with air enclosures. The beam which is reflected at R_{2-3} is a superposition of the reflection from glass-air and glass-sample
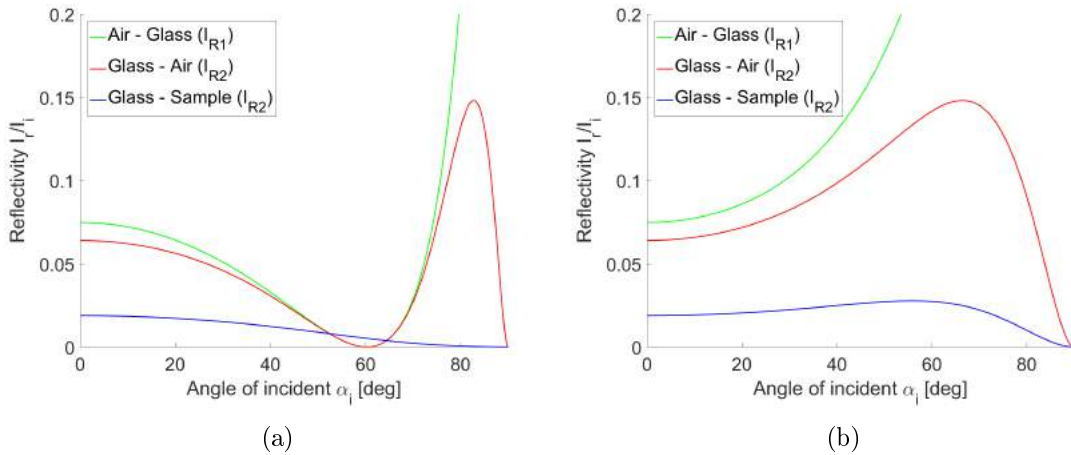

Figure 5.3: (a) P-Polarised reflectivity at different angles of incident and transitions from Glass-Air, Air-Glass, Glass-Sample, according to figure 5.2 (b) S-Polarised reflectivity.

In order to investigate the behaviour of these reflections, the intensity of the reflected beam (I_{R2}) was calculated using Jones formalism for both, the reflection of air n_3 =1.0 and sample with an assumed refractive index $n_3 = 1.3$. These intensities, normalized by the intensity of the illumination beam I_i, are plotted in figure 5.3 for angles of incidence between $0 \leq \alpha_i \leq 90°$. Here, the glass plate was chosen to be a sapphire glass, which has a refractive index n_2= 1.7526 at a wavelength of 785 nm [41].

Figure 5.3 (a) reveals that when the glass plate is illuminated at the Brewster angle, both reflections from air-glass (Green curve) and glass-air (Red curve) vanish. In

contrast, the reflection of the transition from glass to the sample does not vanish completely (Blue curve). Consequently, as long as the setup's detecting system has at least a resolution from the dimension of the air enclosures, this fact can be used to unambiguously filter out the reflection from the sample, and therefore, with help of Fresnel's equations, determine the sample's refractive index.
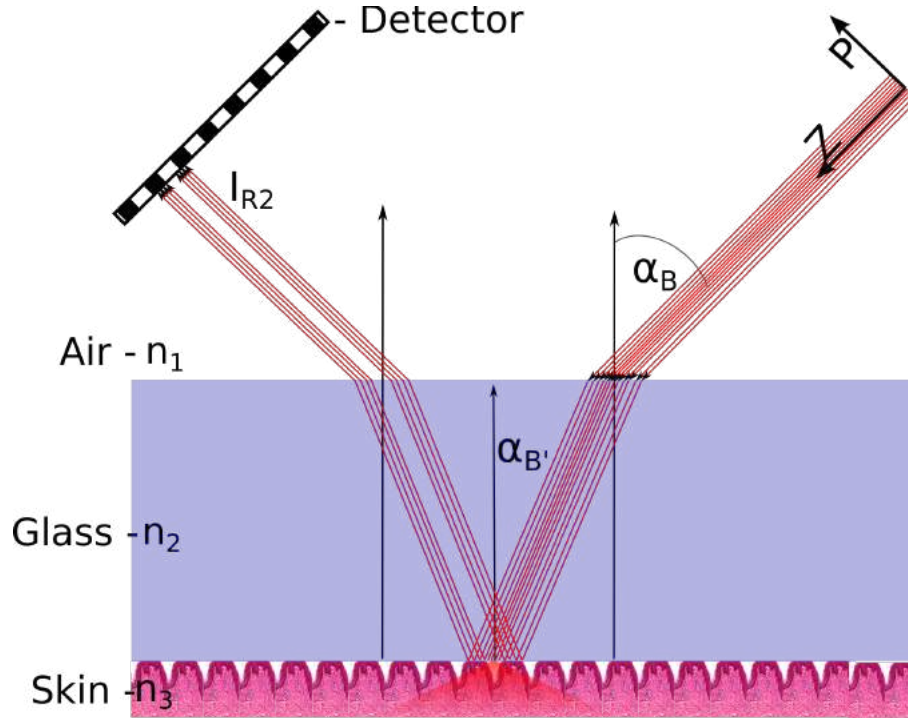

Figure 5.4: Sketch of a samples reflection with air enclosures. When the glass plate is illuminated at the Brewster angle, no reflection occurs between the transition of glass to air.

5.2   Monte Carlo Simulations

In order to assessing our approach, Monte Carlo simulations using jamcp3 [13] were performed. Therefore, a sample with cylindrical air enclosures of radius $r = 4$ px was modelled. The covering glass was chosen to be sapphire, where the Brewster angle at a transition form air to sapphire is $\alpha_B = 60.40$. The samples refractive index was chosen to be $n_3 = 1.30$, without any absorption.

The illumination beam's angle of incidence was fixed at $\alpha_B = 60.40$ in order to suppress any reflection at P-Polarisation caused by the air enclosures. The simulations were then performed at P- and S-Polarisation with 10^9 photons each time.

Figure 5.5 shows the surface plot (a) and the top view(b) of the recorded P-Polarised I_{R2_P} intensity profile. The parts within the Gaussian profile, which are zero are caused by the air enclosures. In order to determine the intensity of the reflected beam, the Gaussian profile is fitted by a Gaussian function where the parts corresponding to the presence of air enclosures were excluded from the fitting routine.

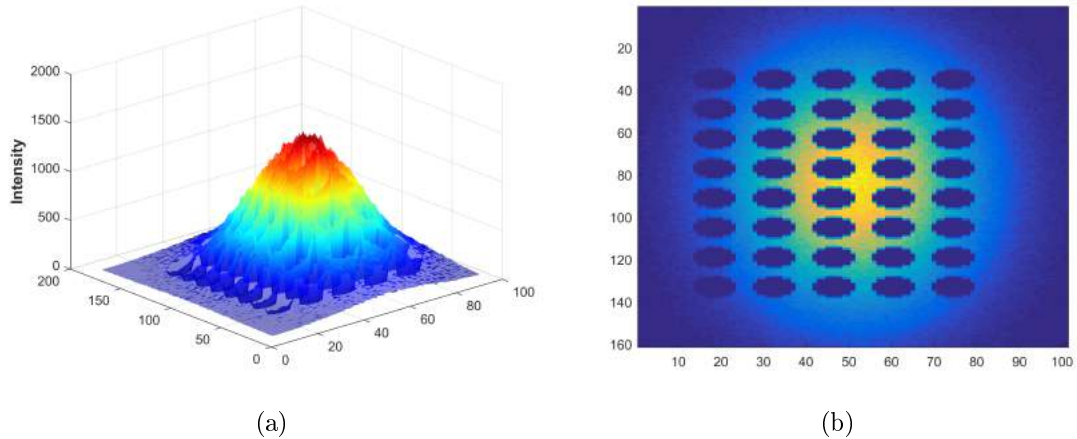(a)   (b)

Figure 5.5: P-Polarisation intensity distribution recorded the reflection of the illumination beam
which propagated through the glass.

Excluding these areas is done in two sequential steps:

- Each pixel where the recorded intensity is lower than a pre defined threshold
  value, is excluded from the fitting routine. Up to now, no algorithm was
  developed to calculate this threshold value. Therefore, the threshold was set
  manually.

- At the boarder of the enclosures, pixel can cover both part of the sample and
  part of the air. Therefore, the recorded intensity of these pixels can be higher
  than the threshold value, but still lower than the value if they would cover
  only the sample. These pixels will falsify the Gaussian fit and therefore lead
  to a wrong intensity value of the reflected beam. To get rid of these pixels, an
  edge detection algorithm (Matlab edge function) was used in order to detect
  air enclosures shapes. This algorithm detects edges in as much as the image
  is analysed in order to find intensity gradients. As a consequence, edges are
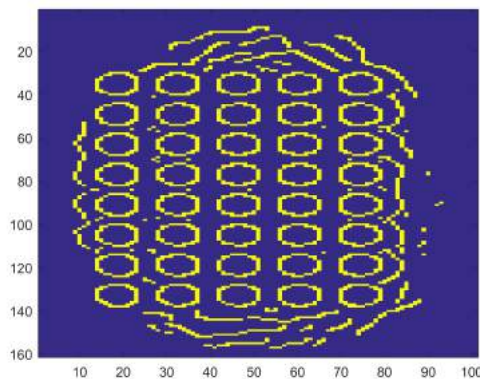 detected independently of their shape. Figure 5.6 shows detected edges in

Figure 5.6: Detected edges in the intensity distribution in order to identify the presence air enclo-
sures.

order to identify the presence air enclosures. The area around these edges
contain potential pixels which cover both, part of the sample and part of the
air. Thence every pixel at the edge and every neighbouring pixel was excluded
from the fitting routine.

Since the sample's position does not change between measuring with P- and S-
Polarised illumination, the same pixels excluded for the P-Polarised reflection are ex-
cluded for the S-Polarised reflection. Figure 5.7 shows the X-Profiles of the recorded
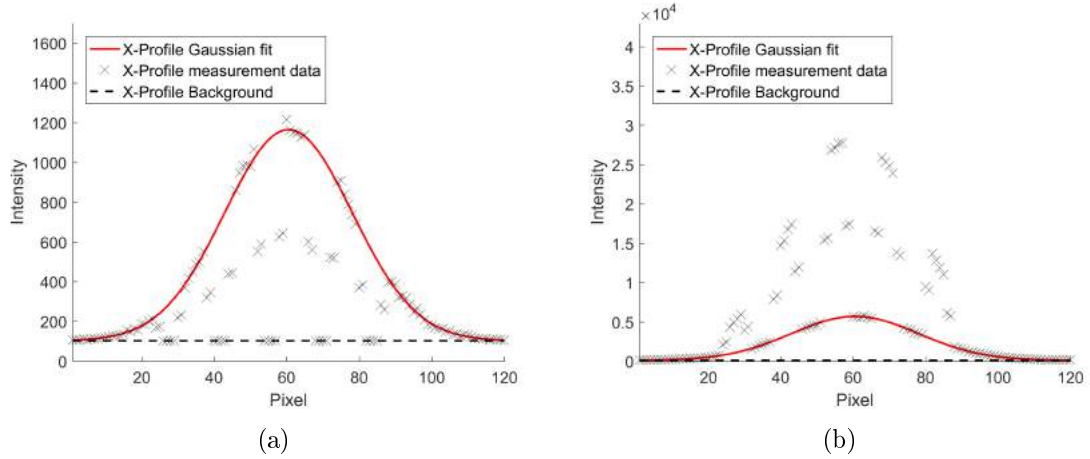

(a)   (b)

Figure 5.7: X-Profile of the P- and S-Reflection

intensity distributions I_{R2_P} and I_{R2_P} with the corresponding fitted Gaussian func-
tion. The pixels with an intensity between the background and the Gaussian function
are caused by pixels covering neither fully the sample nor the air enclosures. How-
ever, it can be seen that for both, the P- and S-Polarisation the applied routine to
exclude the pixels which are not due to the reflection of the sample was successful.
The intensity of the S-Polarised beam, which is directly reflected by the glass plate,
I_{R1_S} is determined by fitting a Gaussian function without excluding any pixels, sim-
ilar to the procedure described in Section 3.4. With these intensities ($I_{R1_p} = 0$),
the equation system 4.6 - 4.8 is solved in order to determine the sample's refractive
index. The results compared with the input parameters can be found in Table 5.1.

	n_3	α_i
Input parameter	1.30	60.40
Determined parameters	1.298±0.008	60.40

Table 5.1: Result of the determined refractive index and angle of incident using jamcp3.

It can be seen that the sample's determined refractive index is in good agreement
with the chosen input parameter. Even if the Monte Carlo simulations were per-
formed in an "idealized" manner, the results reveal the feasibility of filtering air

enclosures and therefore, determining the refractive index of a sample where the surface roughness is not negligible. However, for real skin samples, diffraction effects will occur at the transition from the sample to the air enclosures. As a consequence, air enclosures edge on the recorded image will be blurred. Nevertheless, excluding a broad part around the edges from the fitting routine will account for these diffraction effects.

Chapter 6

Conclusion and Outlook

In conclusion, measuring the refractive index of highly scattering media by means of imaging in order to filter the backscattered light proved to be an effective manner. In combination with the developed self-calibrating analysis method, refractive index measurements without knowledge of the angle of incidence can be performed in a precision in order of tenths of a percent. However, the accuracy of the imaging setup developed here might be increased by using an imaging detector with a higher resolution. Although the accuracy of refractive index measurements of commonly available reflectometers is about one order of magnitude higher than the setup developed in this thesis, these reflectometers are only able to measure thin sample slices [45]. Further, the detectors typically used in such reflection based refractive index measurements are photodiodes / photomultipliers, where the measured intensity is integrated over a finite area of the same order of magnitude as the illumination beam's diameter [2, 3, 34, 35]. Instead, an imaging sensor was used in this study to record a two dimensional spatial distribution in order to filter out the directly reflected light from backscattered light. As a consequence, the setup can be built in a very compact way and the refractive index of highly scattering samples can be measured in a reliable manner.

In this thesis, the backscattered light was completely filtered out and not further investigated. However, analysing the background could also reveal information about the sample's optical properties. Therefore, a further interesting investigation area is the analysis of the backscattered background.

In a second step, the effect of surface roughness in refractive index measurements was investigated. Therefore, a simple model was assumed where a sample covered with glass contains well defined areas, where the sample directly touches the glass, whereas in some areas air enclosures prevent the sample from direct glass contact. The developed data analysis allowed then to differ the reflections caused by the sample touching the glass and the air enclosures. This method was investigated using Monte Carlo simulations which revealed that this model is a promising way to

measure the refractive index of samples with rough surfaces in a very simple manner. However, the effectiveness of this method needs to be assessed in a further study.

Nevertheless, thanks to the simplicity and compactness of the developed setup in combination with the data analysis, the measurements can be performed in an expeditious manner. Thence, this setup is well suited for scanning applications, *e.g.* 2D scanning of an inhomogeneous samples in order to locate changes in the refractive index.

To my knowledge, accurate measurements of the refractive index of cancerous and healthy skin still remains to be achieved. Thence, the difference in the refractive index for healthy and cancerous skin is still unknown. A promising application of this setup could be the investigation of the refractive index for different skin types. Having an accurate knowledge of the refractive of these tissue types, the refractive index cold be used as a marker of disease.

Bibliography

[1] Z. Wang et. al. *Tissue refractive index as marker of disease* Journal of biomedical optics No. 16; 2011

[2] Qing Ye et. al. *Measurement of the complex refractive index of tissue-mimicking phantoms and biotissue by extended differential total reflection method* Journal of biomedical optics No. 16; 2011

[3] H.Ding et. al. *Determination of refractive indices of porcine skin tissues and Intralipid at eight wavelengths between 235 and 1557 nm* Opt-Soc. Am. Vol. 22, No.6; 2005

[4] E. Gutiérrez-Reyes et. al. *Extension of Fresnel's Formulas for Turbid Colloidal Suspensions: A Rigorous Treatment* Journal of physical chemistry B, No. 118; 2014

[5] Paul A. Tipler, Gene Mosca *Physik, 6.Auflage* 2015

[6] Feynman et. al. *Feynman Lectures on Physics: Volume 2* 1964

[7] J.Peatross and M. Ware *Physics of Light and Optics* Birgham Young University (2013 Edition)

[8] H. Günhan Akarçay et. al. *Monte Carlo modelling of polarized light propagation: Stokes vs. Jones. Part 1* Applied Optics Vol.53 No- 31; 2014

[9] R.C. Jones *A new calculus for the treatment of optical systems* series of eight papers published in the J. Opt. Soc. Am. from 1941 to 1956

[10] Ernst Wilhelm Otten *Repetitorium Experimentalphysik* Springer-Verlag, 2008

[11] D. Stroud *The effective medium approximations: Some recent developments* Superlatices and Microstrucuters, Vol.23, No.3/4, 1998

[12] DMK Deutschschweiz *Formeln, Tabellen, Begriffe* ISBN: 978-3-280-04116-1, 2015

[13] H. Günhan Akarçay *Doctoral Theses: Polarized light propagation in biological tissue.* University of Bern. 2011

[14] L.Brillouin *Wave Propagation and Group Velocity* ISBN: 978-1483253930, 1960

[15] W. Lewin *Lecture Notes Electricity and Magnetism* MIT 1999

[16] C. Greub *Lecture notes Electrodynamics* University of Bern 2013

[17] R. Azzam et. al *Consequences of light reflection at the interface between two transparent media such that the angle of refraction is 45°* Opt-Soc. Am. Vol. 68, No.11; 1978

[18] P. P. Ewald, *On the Foundations of Crystal Optics* (Air Force Cambridge Research Laboratories Report AFCRL-70-0580, Cambridge, MA, 1970).

[19] C. W. Oseen, *Über die Wechselwirkung Zwischen Zwei elektischen Dipolen der Polarisationsebene in Kristallen und Flüssigkeiten*, Ann. Phys. 48, 1-56 (1915)

[20] H. Fearn et. al. *Microscopic approach to reflection, transmission, and the Ewald-Oseen extinction theorem* Am. J. Phys.64, pp986-995 (1996)

[21] M.Mansuripur *The Ewald-Oseen Extinction Theorem* Optics & Photonics News 9, pp 50-55, August 1998

[22] V. C. Ballenegger et. al. *The Ewald–Oseen extinction theorem and extinction lengths* American Journal of Physics, Volume 67, Issue 7, 10.1119/1.19330

[23] P. R. Cooper et. al. *Refractive-index measurements of liquids used in conjunction with optical fibres* Appl. Opt.22 3070–2; 1983

[24] E. Moreels et. al. *Laser light refractometer* Appl. Opt. 23 3010–13; 1984

[25] J Rheims et. al. *Refractive-index measurements in the near-IR using an Abbe refractomete* Measurement Science and Technology Vol.8 Nr.6 pp601

[26] A.Taylor *Illumination Fundamentals* 1st ed. Troy: Renssealer Polytechnic Institute; 2000.

[27] G.Petty *Atmospheric radiation* Second Edition, 2nd Printing, ISBN: 978-0-9729033-1-8

[28] Christian Mätzler, University of Bern. *MATLAB Functions for Mie Scattering and Absorption.* 2002

[29] G.Heritage et. al. *Laser Scanning For The Environmental Sciences* Chichester, UK: Wiley-Blackwell 2009.

[30] P.Stähli *Determining of optical properties of tissues: Setup and optimisation of extinction and double integrating sphere measurements* University of Bern, Bachelor Thesis 2015

[31] N. Sultanova et al., *Dispersion properties of optical polymers*, Acta Physica Polonica A116, 585-587 (2009)

[32] G. M. Hale and M. R. Querry *Optical Constants of Water in the 200 nm to 200 μm Wavelength Region* Applied optics 12, 555 (1973).

[33] W.Heller *The Determinatokin of Frefractive Indices of Colloidal Particles by Means of a New Mixture Rule or from Measurements of Light Scattering* Physical Review, Vol 68 No 1 and 2, 1945

[34] H.Ding et. al.*Refractive indices of human skin tissues at eight wavelengths and estimated dispersion relations between 300 and 1600nm* Phys. Med. Bio. 51, 2006

[35] Teng-Qian Sun et.al. *Measurement of complex refractive index of turbid media by scanning focused refractive index* Optics Letters, Vol 41, No.16, 2016

[36] Thorlabs Inc, *BB3-E03 - Ø3" Broadband Dielectric Mirror, 750 - 1100 nm* `https://www.thorlabs.com/newgrouppage9.cfm?objectgroup_id=139`

[37] SCHOTT optical glass data sheets 2015-07-22

[38] B.W. Pogue and M.S. Patterson, *Review of tissue simulating phantoms for optical spectroscopy, imaging and dosimetry,* J. Biomed. Opt. 11, 041102 (2006).

[39] Florida State University `https://micro.magnet.fsu.edu/primer/anatomy/brightfieldgallery/heavilypigmentedskin20xlarge.html` Jan. 2017

[40] A.J. Welch, M.J.C van Gemert *Optical-thermal response of laser-irradiated tissue.* Second Edition, Springer Verlag

[41] I. H. Malitson and M. J. Dodge *Refractive Index and Birefringence of Synthetic Sapphire* J. Opt. Soc. Am. 62, 1405 (1972)

[42] Dr. H. Guenhan Akarcay University of Bern. *Presentation notes of seminar: Refractive index measurements*

[43] Alf Aesar. *Optical properties of polystyrene latex.* `http://www.alfa.com/content/msds/english/43711.pdf`. July 2015

[44] Oregon Medical Laser Center. *Absorption spectrum of wather.* `http://omlc.org/spectra/water/data/smith81.dat`. August 2015

[45] Surfoptic inc. *Reflectometry Application Note* No. 6

Acknowledgements

First of all I would like to thank Prof. Martin Frenz, who enabled me the possibility to work on this thesis.

I would like to express sincere thanks to Dr. H. Günhan Akarçay for all the support through the whole project. I could benefit a lot from his great experience and patience during the many discussions we had.

Further, I would like to thank all the group members of the institute of Biomedical Photonics, who let me have a look into the research field of Biomedical Photonics.